THERMAL LOSS DETERMINATION FOR A SMALL INTERNAL COMBUSTION ENGINE

THESIS

Joshua A. Rittenhouse, Captain, USAF

AFIT-ENY-14-M-41

DEPARTMENT OF THE AIR FORCE
AIR UNIVERSITY

AIR FORCE INSTITUTE OF TECHNOLOGY

Wright-Patterson Air Force Base, Ohio

DISTRIBUTION STATEMENT A:
APPROVED FOR PUBLIC RELEASE; DISTRIBUTION UNLIMITED

The views expressed in this thesis are those of the author and do not reflect the official policy or position of the United States Air Force, the Department of Defense, or the United States Government.

This material is declared a work of the U.S. Government and is not subject to copyright protection in the United States.

AFIT-ENY-14-M-41

THERMAL LOSS DETERMINATION FOR A SMALL INTERNAL COMBUSTION ENGINE

THESIS

Presented to the Faculty

Department of Aeronautics & Astronautics

Graduate School of Engineering and Management

Air Force Institute of Technology

Air University

Air Education and Training Command

in Partial Fulfillment of the Requirements for the

Degree of Master of Science in Aeronautical Engineering

Joshua A. Rittenhouse, B.S.

Captain, USAF

March 2014

DISTRIBUTION STATEMENT A:
APPROVED FOR PUBLIC RELEASE; DISTRIBUTION UNLIMITED

AFIT-ENY-14-M-41

THERMAL LOSS DETERMINATION FOR A SMALL INTERNAL COMBUSTION ENGINE

Joshua A. Rittenhouse, B.S.
Captain, USAF

Approved:

/signed/	13 Mar 2014
Marc Polanka, PhD (Chairman)	Date
/signed/	13 Mar 2014
LtCol Timothy Radsick, PhD (Member)	Date
/signed/	13 Mar 2014
Maj James Rutledge, PhD (Member)	Date

AFIT-ENY-14-M-41

Abstract

Three analysis techniques were used to measure the heat rejection of a 55 cc air-cooled two-stroke engine. This study was performed as part of a larger effort aimed at extending range and endurance limitations of Group 1 & 2 Remotely Piloted Aircraft (RPA). The engine selected for the study was a 55 cc gasoline-fueled, carbureted, spark-ignition engine made by 3W-Modellmotoren and is representative of RPA engines in these groups. With a surface area to volume ratio of 1.48 $\frac{1}{\text{cm}}$, the engine is in a size region where thermal losses begin to dominate engine efficiency and thermal efficiencies of less than 20% are common. The first measurement method was an energy balance between the fuel energy entering the system and the various avenues for energy to leave the system. The second method used an enclosure around the engine and measured the enthalpy increase of the air flowing past the cooling fins. The third method used heat flux gauges placed on the cylinder head to measure the heat flux at those locations. The energy balance method estimated heat rejection at approximately 30-40% of the total fuel energy for full and partial power settings. As part of the energy balance method, the engines tested achieved a maximum thermal efficiency of 13.7% and a maximum brake power value of 2.9 kW. The engine enclosure method measured heat rejection values to be approximately 2 kW at full and partial power settings. This equates to 8-11% of the fuel energy at full power and 20-26% at a 25% power setting. The heat flux gauge method measured heat flux values of up to 33 $\frac{\text{kW}}{\text{m}^2}$. Applying the heat flux values over the surface area of the cylinder resulted in 1.2-2.1 kW of heat loss. As a percent of total fuel energy this represents 7-13% at full power and 22-30% at a 25% power setting.

I would like to dedicate this thesis to my wife, who is also my best friend. Thank you for your endless love and respect.

Acknowledgments

I would like to acknowledge the support of all those who assisted with the development and execution of this research. This group includes but is not limited to Dr. Marc Polanka, Keith Grinstead, Lt Joseph Ausserer, Capt Alex Rowton, Paul Litke, Dr. Fred Schauer, Maj James Rutledge, LtCol Timothy Radsick, Adam Brown, Jacob Baranski, JR Groenewegen, Ben Naguy, Lt Mark Mataczynski, Capt Travis Husaboe, Lt Kevin Horn, and the rest of the AFRL, ISSI, UDRI, and AFIT team. I would like to specifically thank Rich Ryman for assisting in various aspects of setting up the test bench, Rob Free and Dr. Rich Anthony for all their support with the heat flux gauges, and Dave Burris for designing and coding the LabVIEW control and data acquisition programs.

Joshua A. Rittenhouse

Table of Contents

Page

List of Figures

List of Tables

List of Symbols

Symbol	Definition
c_p	Specific heat capacity at constant pressure
dx	Thickness of Kapton in heat flux gauges
$\dot{E}_{e,k}$	Exhaust kinetic energy flux
E_t	Total energy
$\dot{H}_e$	Exhaust gas enthalpy flux
$\dot{H}_{e,ic}$	Exhaust chemical enthalpy flux due to incomplete combustion
$\dot{H}_{e,s,a}$	Exhaust sensible enthalpy flux entering atmosphere
k	Thermal conductivity
$\dot{m}_{air}$	Air mass flow rate
$\dot{m}_f$	Fuel mass flow rate
N	Engine speed
n_c	Revolutions per cycle
P_b	Brake power
P_i	Indicated power
P_{pf}	Piston friction power
P_{tf}	Total friction power
p	Pressure
$\dot{Q}$	Heat transfer rate
Q''	Heat flux
$\dot{Q}_{c,e}$	Heat-transfer rate to coolant in exhaust ports
$\dot{Q}_{cool}$	Heat-rejection rate to coolant
$\dot{Q}_{e,r}$	Heat flux radiated from exhaust system
Q_{LHV}	Lower Heating Value

Symbol	Definition
$\dot{Q}_{misc}$	Miscellaneous energy fluxes and transfers
$\dot{Q}_w$	Heat-transfer rate to combustion chamber walls
R	Resistance
R_0	Resistance at calibration temperature
r_c	Compression ratio
$\bar{S}_p$	Mean piston speed
T	Temperature
V_c	Combustion chamber volume
V_d	Displacement volume
$W_{c,i}$	Indicated work per cycle
α_R	Temperature coefficient
η_f	Fuel conversion efficiency
η_{th}	Thermal efficiency
γ	Specific heat ratio
τ	Torque

List of Acronyms

Acronym	Definition
AFRL	Air Force Research Laboratory
ATDC	After Top Dead Center
BTDC	Before Top Dead Center
AFR	Air-to-Fuel Ratio
AKI	Anti-Knock Index
BDC	Bottom Dead Center
BMEP	Brake Mean Effective Pressure
BSFC	Brake Specific Fuel Consumption
CI	Compression-Ignition
CN	Cetane Number
CFM	Cubic Feet per Minute
DAQ	Data Acquisition
DI	Direct Injection
DOD	Department of Defense
FMEP	Friction Mean Effective Pressure
HCCI	Homogeneous Charge Compression Ignition
IC	Internal Combustion
IMEP	Indicated Mean Effective Pressure
IR	Infrared
JP8	Jet Propellant-8
LHV	Lower Heating Value
MON	Motor Octane Number
PRF	Primary Reference Fuel

Acronym	Definition
RON	Research Octane Number
RPA	Remotely Piloted Aircraft
RTD	Resistance Temperature Detector
SERL	Small Engine Research Laboratory
SI	Spark-Ignition
TDC	Top Dead Center
VFD	Variable Frequency Drive
WOT	Wide Open Throttle

THERMAL LOSS DETERMINATION FOR A
SMALL INTERNAL COMBUSTION ENGINE

I. Introduction

Advances in reciprocating Internal Combustion (IC) engine technology have been slow to spread to engines on the smaller end of the size scale. This research aims to provide experimental data and contributions to the study of engines used in Remotely Piloted Aircraft (RPA) applications.

1.1 Motivation

The top expense in the U.S. Air Force is the cost of fuel. The Department of Defense (DOD) has long desired use of a single battlespace fuel such as Jet Propellant-8 (JP8). Additionally, RPA flights are limited in range and endurance by how efficiently they use their onboard fuel. Logical conclusions drawn from these statements is to increase fuel efficiency while converting engines to operate on JP8. Applying this conclusion to the area of small RPA engines is the primary motivation of this research.

While larger RPAs have been able to rely on JP8-fueled turbine engines, small RPAs still take advantage of the larger power-to-weight ratios of reciprocating IC engines. These engines are typically fueled by gasoline, ignited by a spark, and operate on either a two or four-stroke cycle. Compression-ignition diesel engines as seen in the automotive industry can easily operate on JP8, but are not commonly used in aviation because of their lower specific power values (power-to-weight). RPA engines are rarely purpose-built and are often taken from the model aircraft industry. Performance data on these engines is often limited to manufacturer rated power output at a given engine speed.

1.2 Objectives

There are two overarching Air Force goals that this research is designed to support, increased fuel efficiency and use of a single battlefield fuel. Due to the limited amount of engine performance data on small RPA engines, additional baseline characteristic testing must be performed before improvements can be made. As a step towards establishing baseline characteristics, this research is focused on the following objectives:

1. Evaluate techniques for measuring heat rejection on a small reciprocating engine.

2. Characterize the heat rejection on a small reciprocating engine as a fraction of total energy usage.

Heat rejection or thermal loss characterization is useful in several areas. The design and sizing of radiators, oil coolers and air cooling ducts are all dependent on the amount of desired heat rejection from the engine. In an effort to increase efficiency, techniques can be made to minimize the amount of heat rejection. Conversely, high levels of heat rejection could possibly lower combustion chamber temperatures to aid in avoiding precombustion.

1.3 Methodology

The first step in achieving the specified research goals was to research what has already been done in this field of study and determine applicable techniques for quantifying the amount of heat loss from a small air-cooled engine. Once this initial investigation had been performed, a small engine test bench was then configured to evaluate the selected measurement techniques. The data collected from the different techniques was then compared to anticipated conservation of energy results and to data collected on other engines. Once the data was determined to be repeatable, relationships were drawn between the amount of heat rejection and engine control variables such as power, speed, and cooling airflow.

1.4 Organization

This chapter serves as an introduction to the research presented in this thesis and to outline the objectives and methodology used. Chapter II provides the technical basis for the research performed through the description of several fundamental concepts. Additionally, Chapter II references several published research efforts relevant to this research. Chapter III is a detailed description of the experimental setup, test configurations and instrumentation used. Experimental results and analysis are discussed in Chapter IV along with mention of any configuration changes and problem areas. Chapter V summarizes the recommendations and conclusions of the analysis described in the previous chapter. Chapter V also provides recommendations for future research in the area of small engines.

II. Background and Theory

This chapter establishes the fundamental concepts of internal combustion engines with a focus on efficiency and measuring thermal losses or heat rejection. The objectives of this research are to evaluate different heat rejection measurement techniques and to use those techniques in characterizing the thermal loss of a 55 cc 2-stroke RPA engine. A brief overview of reciprocating engines is provided, followed by a thermodynamic discussion on ideal and actual engine efficiency. Several approaches to measuring the amount of heat rejection are also discussed before closing the chapter in how other research efforts have made use of heat rejection data. References to related research as well as relevant engineering formulas are provided throughout the chapter.

2.1 Reciprocating Internal Combustion Engines

Reciprocating engines utilize a piston within a cylinder body to carryout the sequences essential to any IC engine operation. The standard IC engine processes include air intake, compression, combustion and expansion. Variations in IC engines can be categorized in how each executes these fundamental processes. The following subsections discuss the various differences in reciprocating engines.

2.1.1 Engine Cycles.

There are two main types of engine cycles found in reciprocating engines, two-stroke and four-stroke. Each operating cycle is named for the number of upward and downward sweeps or strokes of the piston per power cycle. The main differences between the two cycles is in the gas exchange process within the cylinder. The four-stroke uses one downward stroke of the piston to create a volume of low pressure that draws in a fresh charge of air and fuel. The following stroke is used to compress the gas mixture. The charge is then ignited and allowed to expand during the second downward stroke. The last

stroke uses the upward motion of the piston for a complete evacuation of the exhaust gases. Four-stroke engines are characterized by reliable and fuel-efficient operation with minimal emissions.

Two-stroke engines complete the same sequence of events with a few differences. A fresh charge of air is pushed into the cylinder from the crankcase due to the downward motion of the piston moving into the crankcase. Exhaust gases from the previous cycle are pushed out the cylinder through the exhaust port as the fresh charge enters through a scavenging port. Since the exhaust port is open as the fresh charge enters, it is normal for some of the fresh charge to escape through the exhaust port in what is known as short-circuiting. As the piston travels upward, both the scavenging and exhaust ports of the cylinder are closed and the charge begins to compress. Towards the top of the stroke, the charge is ignited followed by the expansion stroke. As the piston travels downward, the exhaust and scavenging ports are uncovered starting the gas exchange over again. Two-stroke engines are characterized by high specific power values and simple design features.

Both two and four-stroke cycles can be run using atmospheric air (naturally aspirated) or using pre-compressed air. The air can be compressed using an engine driven compressor (supercharger) or by means of an exhaust turbine driven compressor (turbocharger). The compressed air has a higher density that allows for a larger mass of air to be drawn into a cylinder of set size. Additional fuel is added to balance the increased air mass into stoichiometric proportions. The result is larger power values over naturally aspirated engines without an increase in displacement or compression ratio at the cost of incorporating an additional engine component.

2.1.2 Ignition Types.

The ignition of a fuel air mixture occurs once enough energy has been added to a cylinder to allow for combustion. Gasoline engines typically rely on the combined energy of the compression provided by the piston and the the spark of a spark plug. The spark

adds the final amount of activation energy necessary for combustion in what is commonly referred to as Spark-Ignition (SI). SI engines however, will not reliably ignite unless the air and fuel mixture at the spark plug is consistently mixed to proportions within the lean/rich flammability limits [17]. The fuel is often mixed with the air prior to entering the cylinder for a homogeneously mixed charge with an Air-to-Fuel Ratio (AFR) that is within these limits.

Compression-Ignition (CI) relies fully on the added energy from the compression of the cylinder. As the cylinder is compressed, the temperature of the charge increases to the point where a fuel-air mixture is able to ignite. In order to control a CI engine, the fuel is usually withheld from the cylinder until the combustion event is desired as in diesel engines. Similarly, the fuel in a gas turbine engine is also withheld as air is first compressed to ratios as much as 40:1. In an attempt to capture the efficiency benefits of high compression and the reduced emission benefits of premixed SI engines, researchers continue to strive towards perfecting what is known as a Homogeneous Charge Compression Ignition (HCCI) engine. An HCCI engine uses compression ignition on a premixed charge. The difficulty of HCCI operation is in timing control of the ignition event.

2.1.3 Fuel Delivery.

SI engines have historically relied on carburetors to control and meter the air and fuel. As air enters the carburetor, it travels through a converging-diverging Venturi [13]. Following Bernoulli's principle, the air velocity increases and the static pressure decreases. The decrease in pressure draws fuel into the air stream through a jet. The fuel vaporizes as it is introduced into the air flow path resulting in a homogeneous fuel-air mixture prior to entering the cylinder. This technique requires fuels with a high volatility. A throttle plate is placed downstream of the Venturi to control airflow into the cylinder by restricting the intake path. Reduced airflow through the Venturi results in reduced fuel being introduced into the air stream, thus adjusting the AFR at the cost of increased pumping losses for the

engine. Additional jets and metering circuits are added to further adjust flows depending on the level of loading. During cold-starts, fuel vaporization is decreased from normal operation. To increase the amount of vaporized fuel in the air and allow for smoother low temperature operation, additional fuel is added at the carburetor [15]. A choke plate is placed upstream of the Venturi to create this rich mixture. By restricting flow upstream, the choke plate can be used to further reduce the pressure in the Venturi resulting in increased fuel flow.

More recently, carburetors are being replaced by fuel injection systems in SI engines. A fuel injector acts as a valve to control the flow of pressurized fuel into an intake port or with higher pressures directly into the cylinder. Direct Injection (DI) allows for a stratified charge in which the fuel is not homogeneously mixed with the air. Fuel is injected in such a way as to ensure an ignitable mixture at the spark plug. DI thus allows for leaner combustion than previously capable in SI engines [7]. Another benefit to DI is seen in two-stroke engines as a way to avoid short-circuiting [7]. Through DI, fuel can be injected after the exhaust port is closed to avoid any loss of fuel out the exhaust.

Rather than controlling engine speed by restricting the airflow, CI engines control engine speed by controlling fuel delivery. CI rely on the precise timing of directly injecting fuel into the cylinder in order to control combustion. The ratio of fuel to air is not as crucial to ignition because as the fuel is injected there is always a region between the fuel and air within the flammability limits. In addition, the energy required to ignite the mixture is present everywhere in the combustion chamber rather than localized at the location of the spark plug as in an SI engine. This fuel delivery technique avoids pumping losses by allowing free flow of the intake air.

2.2 Engine Efficiency

2.2.1 Otto Cycle.

Maximum thermal efficiency is limited by the idealized thermodynamic Otto cycle. Accounting for combustion efficiency, the fuel conversion efficiency, η_f is calculated as the ratio of power output versus the fuel energy used.

$$\eta_f = \frac{P_b}{\dot{m}_f \cdot Q_{\text{LHV}}} \tag{2.1}$$

where P_b is the measured brake power output of the engine crankshaft. The thermal energy is provided through the combustion of a given fuel as calculated by the product of fuel mass flow rate, $\dot{m}_f$, and the lower heating value, Q_{LHV}, of the fuel.

A pressure-volume plot of the ideal Otto cycle is shown in Figure 2.1 [12]. The amount of work output from the cycle is seen from the enclosed area. The lower boundary from state 2 to 3 is the isentropic compression stroke. Heat is added through combustion at state 3 for an increase in pressure at constant volume to state 4. The system is brought to state 5 through the isentropic expansion power stroke. Heat is then released at constant volume to bring the system back to state 6.

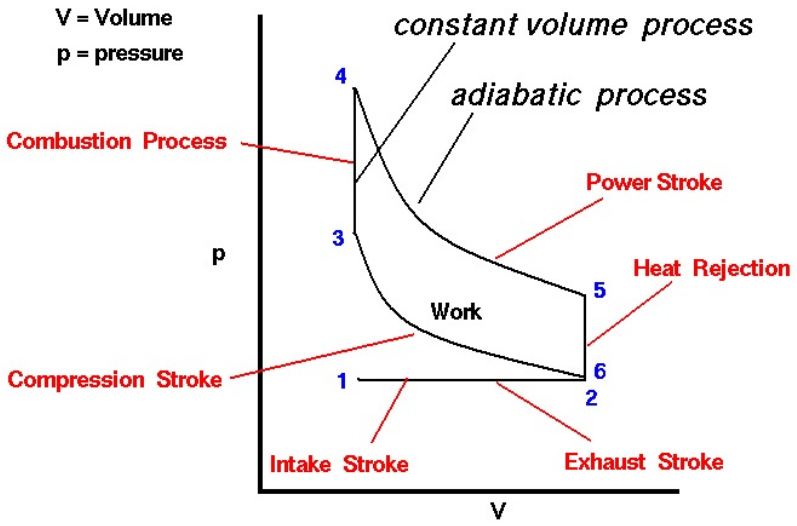

Figure 2.1: Pressure-Volume diagram of ideal four-stroke Otto cycle [12]

The Otto cycle defines the maximum ideal thermal efficiency of a spark-ignition reciprocating engine as a function of compression ratio, r_c, and specific heat ratio, γ. The specific heat ratio for air is 1.4 at standard conditions and decreases slightly as temperature rises through the compression and combustion process to as low as 1.2. The geometric compression ratio is set by engine geometry as the ratio between the combined volume of the cylinder and combustion chamber when at the bottom of the stroke Bottom Dead Center (BDC) versus the remaining volume of the combustion chamber when at the top of the stroke Top Dead Center (TDC). As the piston moves upward from BDC, the scavenging or exhaust ports may not be closed yet, therefore delaying compression. Alternatively, the adjusted compression ratio based on port closings is the effective compression ratio. Effective compression ratio is ratio of the combined volume of the cylinder and combustion chamber once all ports are closed versus the volume of the combustion chamber at TDC. The governing efficiency equation is then [6]:

$$\eta_{th} = 1 - \frac{1}{r_c^{\gamma-1}} \tag{2.2}$$

where the effective compression ratio is used for r_c in this effort. For modern gasoline-fueled, spark-ignited engines, compression ratios are normally around 10:1, but can be as high as 14:1. For a compression ratio of 10:1 and using an approximate average γ of 1.35 over the temperature range, the maximum theoretical efficiency is calculated to be approximately 55% as seen in Figure 2.2

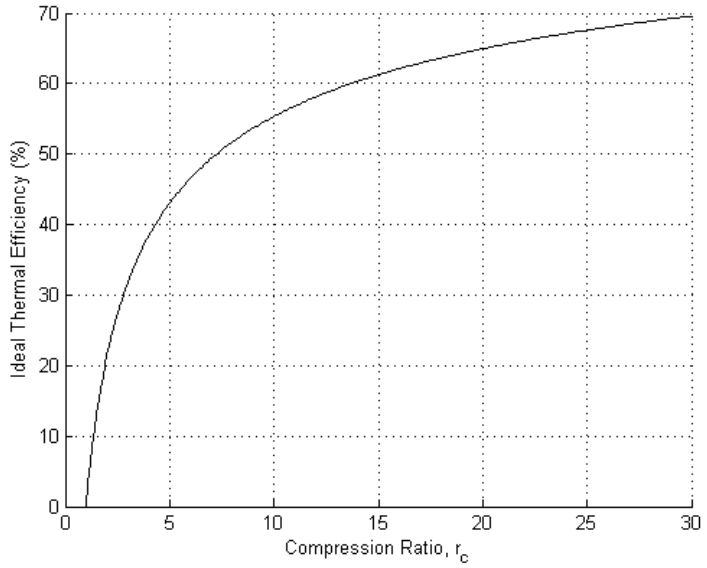

Figure 2.2: Ideal Otto thermal efficiency for range of compression ratios, $\gamma = 1.35$

2.2.2 Efficiency Losses.

Actual engine efficiencies are much lower than the theoretical maximum given by Equation 2.2. There are several reasons why this is the case. For one, the compression and expansion strokes are not isentropic. One of the largest contributors to less than ideal efficiency is thermal loss through the cylinder body, typically 20-36% of the fuel heating value [6]. Taylor describes the main losses in three terms, time loss, heat loss, and exhaust

loss [16]. Time loss is the loss of work due to non-instantaneous combustion. Heat loss is the loss of work due to heat rejection through the cylinder walls. Exhaust loss is the loss of work from the opening of the exhaust valve before BDC.

Thermal energy lost through engine cylinder walls is a major component of both overall engine efficiency and engine thermal management. Increased surface area within the cylinder allows for increased heat transfer to the cylinder walls. As cylinder size decreases, the ratio of surface area to volume increases resulting in increased thermal losses [6]. This phenomenon is shown in Figure 2.3 which shows the trend in power versus cylinder surface area to swept volume ratio for a range of IC engines. The points are manufacturer specified power values collected from over fifteen different manufacturers. The ratio was calculated using the engine stroke and bore size.

$$\frac{\text{Surface Area}}{\text{Displacement Volume}} = \pi \cdot \text{Bore} \cdot \left(\frac{1}{2} \cdot \text{Bore} + \text{Stroke} \right) \tag{2.3}$$

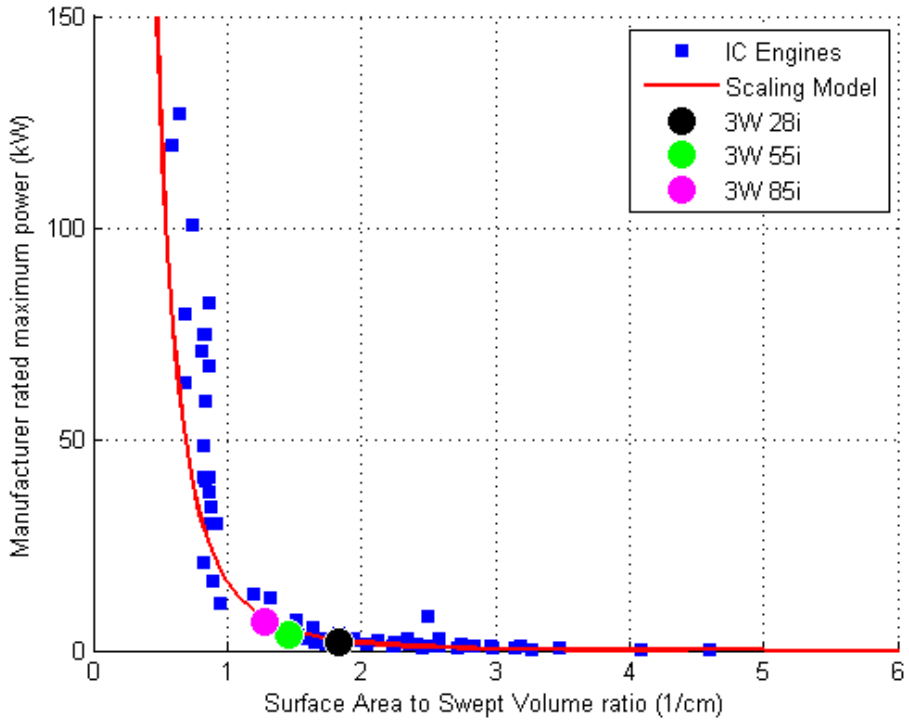

Figure 2.3: Manufacturer rated IC engine power vs. cylinder surface area to swept volume ratio

The loss of unburned fuel exiting the exhaust in two-strokes is a combination of short-circuiting and incomplete combustion. Incomplete combustion is approximated to be less than 5% while running at lean or stoichiometric mixture conditions [6]. Figure 2.4 shows a plot from Heywood providing combustion efficiency as a function of exhaust equivalence ratio [6]. As equivalence ratio increases beyond a value of 1.0 combustion efficiency decreases dramatically. A Proper carburetor tuning is key to minimizing the introduction of excess fuel that cannot be burned. The combined loss of short-circuiting and incomplete combustion could be measured through the addition of emission instrumentation in the exhaust.

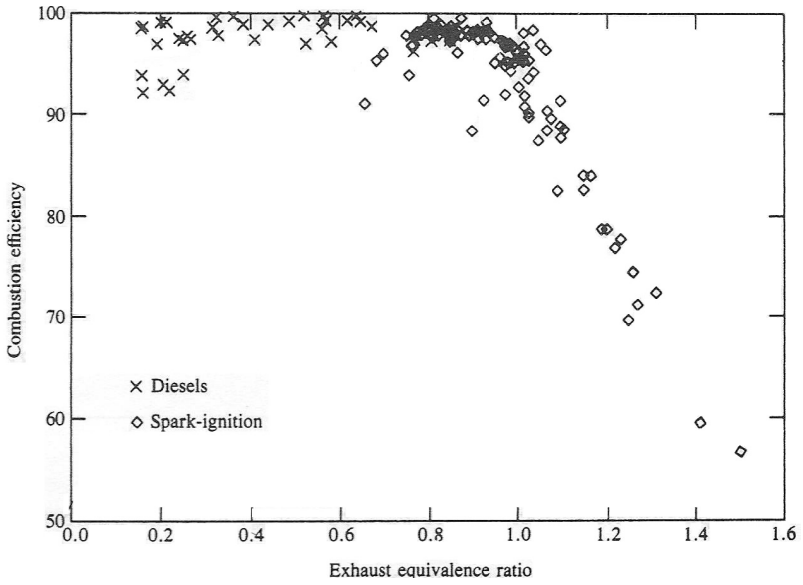

Figure 2.4: Combustion efficiency as a function of exhaust equivalence ratio [6]

Two-strokes suffer from an additional fuel conversion efficiency loss over four-strokes known as short-circuiting. Short-circuiting is the escaping of fresh fuel/air charge through the exhaust port during the gas exchange process. This loss is of order 20% [7] of the fresh charge, a substantial area of loss for two-stroke engines. Improved scavenging will minimize short-circuiting thus reducing fuel consumption and hydro-carbon emissions [7]. Short-circuiting losses are highest at low loads and can be reduced over a small range of engine speeds by utilizing a tuned exhaust pipe. Kumarappa and Prabhukumar [9] saw a 9.1% increase in efficiency by implementing a direct injection fuel system to avoid any short-circuiting effects. Being able to quantify the loss mechanisms is critical to developing methods to improve overall efficiency.

The pressure-volume diagram for a two stroke cycle is set by the locations of the exhaust port and scavenging port. Figure 2.5 shows a two-stroke p-V diagram with vertical lines representing the point during the compression and expansion strokes where the ports

are opened and closed. Starting on a an upward stroke from BDC, all ports are initially open. The first to close is the scavenging port (SC) followed shortly after with the exhaust closure (EC). The piston travels to TDC and starts the return to BDC with both ports closed. Because of the fixed geometry of the ports, the exhaust port is first to open (EO) because it was the last to close. The scavenging port is opened (SO) shortly after the exhaust followed soon after with the piston hitting BDC. The combustion chamber volume is indicated with V_c and the displacement volume with V_d.

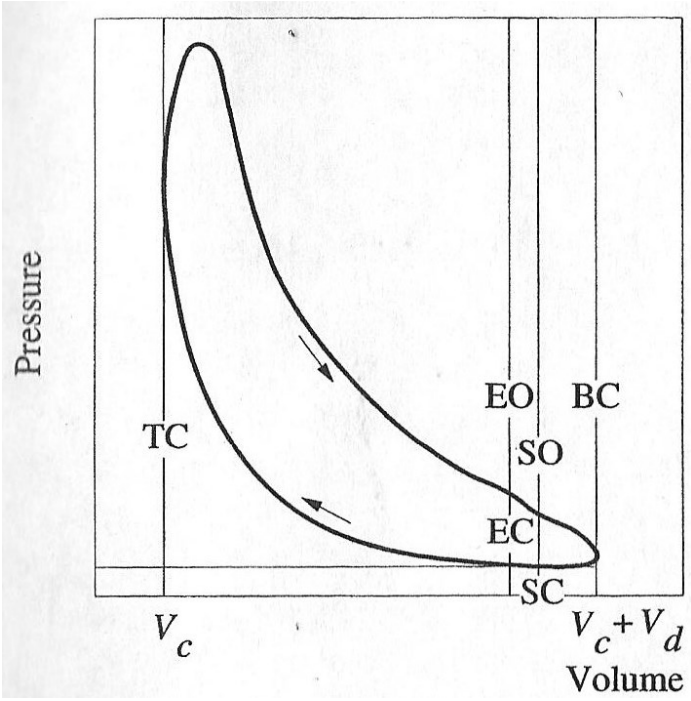

Figure 2.5: Actual two-stroke pressure-volume diagram [7]

In-cylinder pressure data are valuable for determining indicated work over the operating cycle of an internal combustion engine. The indicated work per cycle is a measure of how compression, combustion, and expansion processes affect the power output of an engine. It is a sum of work available at the crankshaft and the work required to

overcome engine friction and pumping power [6]. Conveniently, indicated measurements are not dependent on drivetrain components connected to the engine, so compensation for additional frictional loading is not necessary when recording data. The AVL IndiCom combustion analyzer is designed to measure and record high speed pressure data during engine operation. This data, along with a high-resolution crank angle position signal, can yield indicated work per cycle via the following equation

$$W_{c,i} = \oint p \, \mathrm{dV} \tag{2.4}$$

Subsequently, indicated power output can be obtained with the following equation

$$P_i = \frac{W_{c,i} \cdot N}{n_c} \tag{2.5}$$

In-cylinder pressure measurements are also used to signify the presence and severity of knock in an engine. During normal engine operation, a trace of in-cylinder pressure versus crank angle shows a smooth rise and fall over the engine's compression and expansion strokes. If an engine knocks however, the pressure trace will show sharp peaks and valleys in an oscillatory manner. These sharp pressure spikes can damage an engine's internal and structural components over time, so it is necessary to precisely determine the point of onset of knock in a particular engine in terms of fuel AKI or spark timing in spark-ignition engines.

2.2.3 Fuels.

The limiting factor in increasing the compression ratio for increased efficiency is the ability of the fuel to avoid compression ignition. Gasoline fuels are rated for their ability to avoid compression ignition and resistance to knock. The Research Octane Number (RON) is measured through a research method (ASTM D-2699) and the Motor Octane Number (MON) is measured under more severe operating conditions (ASTM D-2700) [6]. Averaging these two ratings is the Anti-Knock Index (AKI) as seen at gas stations pumps

in the US.

$$\text{AKI} = \frac{\text{RON} + \text{MON}}{2} \tag{2.6}$$

Using fuels with lower AKI values increases the risk of surface-ignition and subsequent knock. One method of compensating for the lower AKI is to reduce engine temperature in order to avoid surface-ignition prior to spark ignition. This conflicts however with the goal of improved efficiency through minimizing heat loss.

Fuels such as diesel or JP8 used in compression ignition engines are rated differently. Compression ignition engines require fuel which ignites easily under compression with minimal ignition delay. These fuels are tested and rated with a Cetane Number (CN) value from 0-100 to describe how well the fuel meets these characteristics. Cetane ignites very easily under compression and is assigned a CN of 100. A higher CN relates to easier combustion and shorter ignition delay.

2.3 Applications to Characterized Heat Rejection

Thermal energy lost through engine cylinder walls is a major component of both overall engine efficiency and engine thermal management. Small engines suffer from large surface area to volume ratios resulting in increased thermal losses over larger engines [6]. For engine efficiency, thermal loss through the cylinder walls is a negative aspect in that the heat is energy not available as useful mechanical work. For thermal management, thermal loss is a positive aspect in that it results in lower cylinder temperatures. Thermal losses through the cylinder body allow engine components to cool and stay within acceptable operating ranges. Higher temperatures cause fatigue cracking, deteriorate lubricating oil film, and abnormal combustion [6]. Temperature distribution is not even throughout the cylinder body. Locations of consistently elevated temperatures with respect to the rest of the cylinder are referred to as hot spots. In addition to increased fatigue at these locations, hot spots can ignite the fuel/air mixture separately from the spark plug. This results in an abnormal combustion event known as surface-ignition and can cause engine knock [6].

Avoiding knock is one of the main obstacles to overcome when converting an engine to run on a low AKI fuel.

The DOD uses small engines in RPA applications and has been interested in the use of heavy fuels for both decreased Brake Specific Fuel Consumption (BSFC) and reduced fuel delivery logistics. Avoiding surface-ignition is difficult when converting an existing gasoline-fueled, spark-ignition engine to a low octane or heavy fuel. Heavy fuels have less resistance to compression ignition and are therefore already more prone to pre-ignite in an engine that compresses the fuel/air mixture. Wilson [18] however, was successful in transitioning a gasoline 34 cc four-stroke to operate on zero-octane fuel (n-Heptane) with negligible knock and a 4.1% decrease in BSFC. Ease in transition was attributed to both a low compression ratio (8:1) and a high surface area to volume ratio (1.7). Conversely, running heavy fuel in a gasoline engine that is too cool will prevent the fuel from vaporizing to create a combustible air-fuel mixture. To overcome this scenario as seen in cold-starts, Groenewegen ran an engine initially on gasoline before switching to JP8 [5].

High thermal losses are being utilized in other ways besides minimizing knock and component fatigue. Martinez-Frias et al. showed how proper management of heat loss can be used to control a HCCI engine [10]. This type of engine uses a premixed charge like in gasoline engines but uses compression ignition as in diesel engines. The result is a highly efficient engine with low emissions. Through managing thermal losses, the point of ignition is controlled. Similarly, Mueller et al. demonstrated that the thermal losses can be used to reduce automotive engine emissions where engine operation duration is short [11]. Both of these applications would benefit from accurately quantifying thermal losses.

Ajav, Singh, and Bhattacharya [2] used cooling water and a series of thermocouples in studying how ethanol-diesel blends affected thermal losses in a compression ignition engine. They categorized thermal loss into four areas: heat lost to the cooling water, heat lost to the exhaust gases, heat lost to the engine oil, and miscellaneous thermal loss. Using

diesel fuel, they measured 36.5% of the fuel heating value being rejected as heat through the cooling water and engine oil.

2.4 Research Gap

The topics in this chapter provide a background in heat rejection of IC engines. Still limited information is available regarding how much of this can still be applied to small two-stroke engines. A research gap exists in fully characterizing the small two-stroke engines being used in RPAs. The focus of this research was to fill this gap by evaluating techniques for measuring heat rejection and then characterizing the heat rejection on a small two-stroke engine.

III. Experimental Setup

This chapter provides a description of the facilities, instrumentation, and configuration for the experiments performed as part of this research. Three different techniques were used to measure the amount of thermal heat loss from the cylinder: Energy Balance, External Flow, and Heat-Flux Sensors. In order to execute these measurement techniques a small engine test bench needed to be constructed. Following test bench setup, initial testing was performed to verify instrumentation configurations and to allow time for modifications. Some of the modifications were part of a specific measurement configuration while others were more general test bench improvements. Experimental configurations are described to clarify the various parameters that were controlled and measured. Instrumentation details are included in this chapter to aid in small engine test bench developments and improvements.

3.1 Small Engine Test Bench

The test bench used in studying the thermal loss techniques was developed in cooperation with the Small Engine Research Laboratory (SERL) of Air Force Research Laboratory (AFRL). The test bench was created as part of a small engine research effort to study thermal and frictional losses with decreasing engine size [3]. An engine was selected near a cylinder surface area to displacement volume ratio of $1.5\frac{1}{\text{cm}}$, the point where thermal and frictional losses begin to dominate combustion physics [6]. The 3W-55i from 3W-Modelmotoren was chosen with a ratio $1.48\frac{1}{\text{cm}}$. 3W-Modelmotoren is a German manufacturer that specializes in engines for model aircraft. The engine as shown in Figure 3.1 is a carbureted two-stroke with mixture adjustment screws for idle and full throttle. Ignition is controlled through the manufacturer ignition module that advances timing as

engine speed is increased. Additional engine parameters are specified in Table 3.1 including a compression ratio of 10:1 [1].

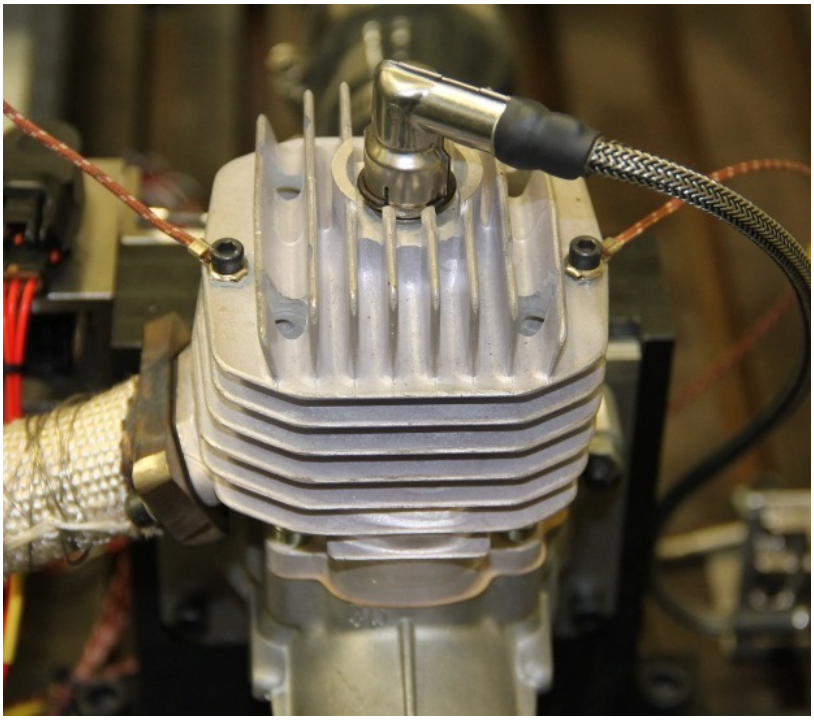

Figure 3.1: Test Engine: 3W-Modelmotoren, Model 3W-55i

Table 3.1: Test engine parameters

Description	Value
Displacement	55 cc
Power	3.9 kW
Mass	1.94 kg
Power Density	2.01 $\frac{\text{kW}}{\text{kg}}$
Bore	45 mm
Stroke	35 mm
Compression Ratio	10:1
Cylinder surface area to volume ratio	1.48 $\frac{1}{\text{cm}}$

The test bench shown in Figure 3.2 was designed to accurately test a family of 3W-Modelmotoren engines with minimal modifications between models. The engine was mounted to the table with cooling air provided by means of a blower (shown on the left). The engine crankshaft was coupled to the drivetrain (located on the right). Intake air was routed through a baffling drum below the table, through a heat exchanger and then brought up to the tabletop and to the engine. Fuel was held in a tank off the table and pressurized with nitrogen to provide flow to the carburetor. A vertical exhaust stack was mounted to the side of the engine at the exhaust port. Data was recorded using a National Instruments FieldPoint system mounted on the bench and routed to a control computer located in an adjacent control room. Additional test bench details are in the following paragraphs and can also be found along with verification results documented in Ausserer et al. [3].

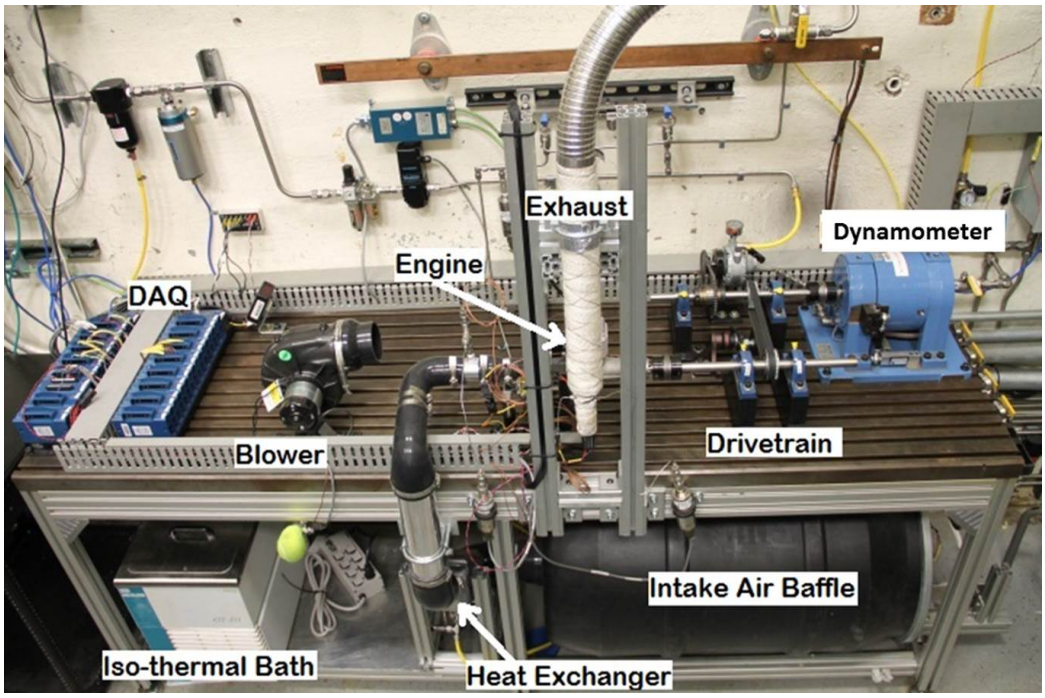

Figure 3.2: Small Engine Test Bench

The intake air control system was designed to compensate for fluctuating air flow and changing ambient air temperatures. A maximum anticipated intake air flow rate was calculated to be 360 $\frac{\text{L}}{\text{min}}$ based on similar engines and maximum delivery ratios for the series of 3W-Modelmotoren engines [3]. A TSI 40211 High Performance Linear Mass Flow Meter was used to measure the flow of intake air at an accuracy of ±3% of the reading. An identical flow meter was later added in parallel to reduce intake air restrictions. The units used a hot wire anemometer and a temperature correction thermocouple to provide a voltage to the Data Acquisition (DAQ) that is proportional to the flow. A 209 L (55 gal.) drum was used as a baffle, isolating the flow meter from oscillating engine air flows. After the drum, air was routed through a Frozen Boost heat exchanger with water as the working fluid. Water temperature was controlled through the use of a Thermo Neslab RTE-211 recirculating isothermal bath. Temperature was measured just prior to the air entering the

engine carburetor with a Type J thermocouple of 2.2 °C or 0.75% accuracy. Pressure was also measured here using a Honeywell TJE pressure transducer with 0.10% accuracy. A 1.6 mm ($\frac{1}{16}$ in.) stainless steel tube was used as a pressure tap to allow the pressure transducer to be mounted to the test bench.

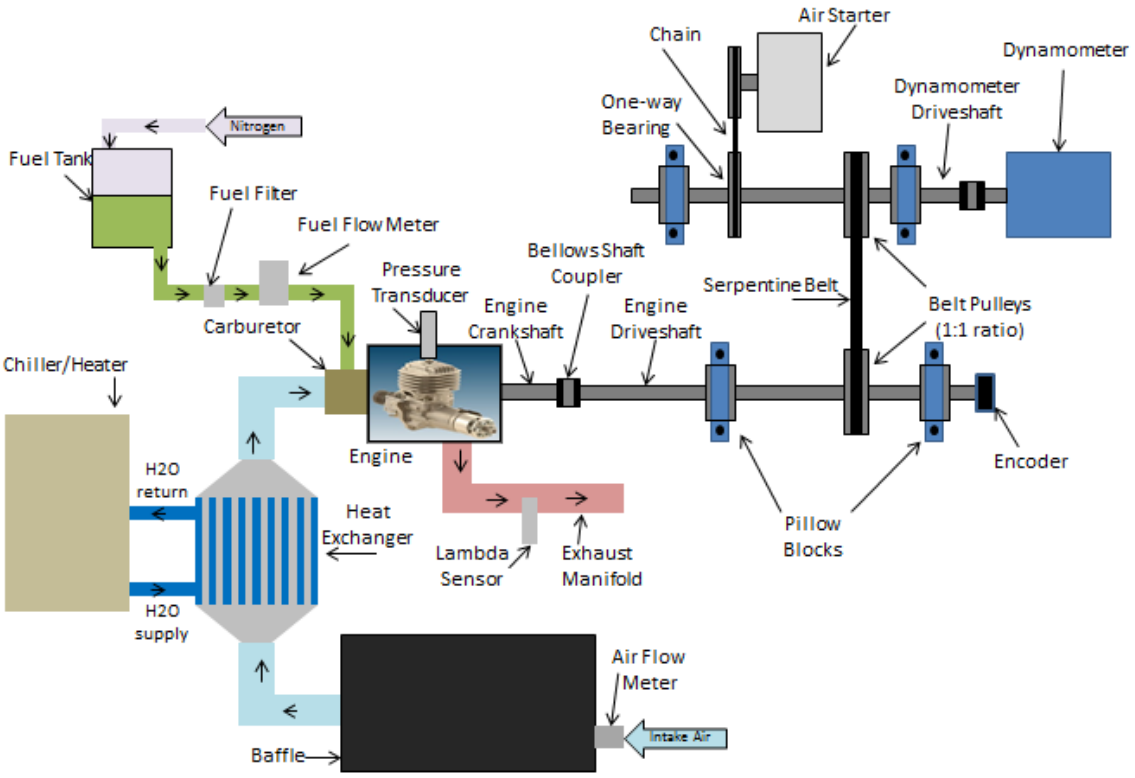

Figure 3.3: Flow of air and fuel in the AFRL Small Engine Test Bench

Fuel flow was anticipated to be on the order of 10's of $\frac{\text{mL}}{\text{min}}$ and was measured using a Max Machinery 213 Piston Flow Meter. The accuracy of the fuel flow meter was ±2% of the reading. The fuel used in this investigation was a Primary Reference Fuel (PRF) blend of 98% isooctane, 2% n-heptane, additionally synthetic 2-stroke oil by volume was added at a ratio of 1:100. The fuel tank was pressurized to approximately 6.7 kPa with nitrogen to provide flow through 40 μm and 7 μm fuel filters and the flow meter to the

carburetor. The AFR was then calculated using the measured air and fuel flow rates. A Powerdex Air-Fuel Monitor by NGK was mounted on the exhaust stack for real-time AFR readings and as a secondary measurement. Temperature and pressure was also measured on the exhaust stack. A Type J thermocouple was inserted into the exhaust stream for exhaust temperatures. This measurement was taken along the fiberglass insulated exhaust pipe at a distance of approximately 15 diameters away from the exhaust port. Exhaust pressure was measured again using a stainless steel tube and Honeywell TJE pressure transducer.

The engine drivetrain was set up as shown in Figure 3.3. Ruland bellows shaft couplers were used to connect the engine crankshaft to the engine driveshaft and the dynomometer crankshaft to the dynomometer. A bellows coupler consists of two shaft hubs joined by a metal bellows for high torsional rigidity. After repeated failures, the bellows couplers were replaced with spider couplers. A spider coupler is made up of two hubs with jaws separated by an elastomer insert or "spider". These couplers are known for their ability to absorb drivetrain shocks. A timing belt pulley system was mounted on pillow block bearings and was used to transfer power to the dynamometer while minimizing vibration. A Magtrol 1 WB 65 eddy current dynamometer measured torque and speed. The dynamometer was capable of measuring up to 10 N-m of torque at up to 10,000 rpm with an accuracy of ±0.5% of the full scale for both torque and speed. A Lubricated Air Motor from GAST was used with a one-way clutch bearing to start the engine by driving the dynamometer driveshaft.

The engine was configured with servo motors for throttle and choke controls. Hitec HS-85MG+ servos were chosen for their high torque and resistance to vibration. In an operational environment, the engine would typically be cooled by airflow from the propeller moving past the cooling fins. On the test bench, cooling for the engine was initially accomplished by means of a JABSCO 35440 series blower directed at the cylinder body. The blower was powered by 24 V DC through the control of a Midwest Motion

Products motor controller. An evaluation of RPAs with engines of similar power ratings to the 3W-55i was done using manufacturer published data. The result was maximum speeds of approximately 30.5 $\frac{m}{s}$ (100 $\frac{ft}{s}$) or less. This speed was used as the maximum velocity for airflow directed at the engine. After the addition of ducting, the blower was found to be incapable of reaching desired flow rates and was replaced by a more capable AC blower. Figure 3.4 shows the air velocities in a 10 cm (4 in.) diameter duct of the different blower configurations.

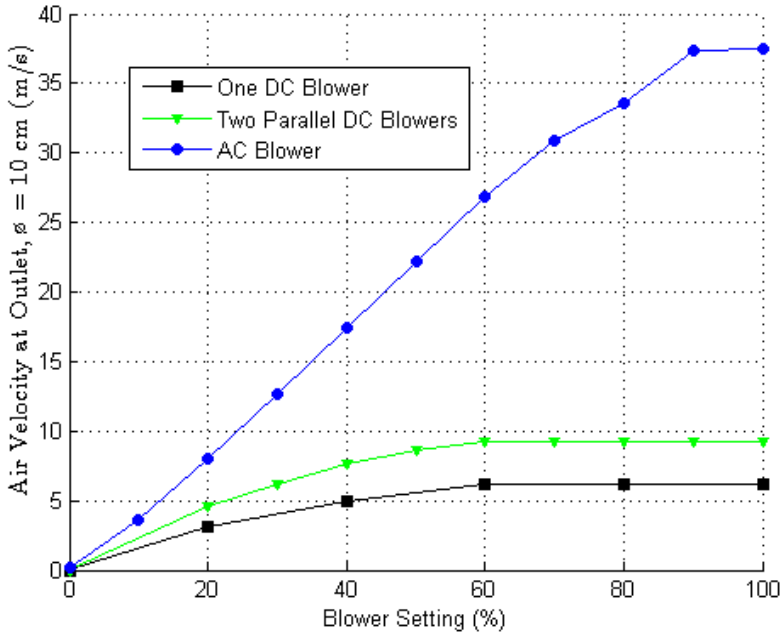

Figure 3.4: Blower velocity tests with DC and AC blower configurations

The AC blower used a 1.1 kW (1.5 hp) 460 V Baldor motor (Model CM3550). This blower was controlled by means of a Baldor Model ID15J403-ER Variable Frequency Drive (VFD) that used a 0-5 V analog input from the DAQ for speed control. Directly coupled to the motor was a Monoxivent D15-3 Blower. The blower is an aluminum alloy,

single-stage, radial-blade blower capable of moving 965 Cubic Feet per Minute (CFM) at 1 inch of static pressure or up to 330 CFM at 7 inches.

Data acquisition was performed using a National Instruments FieldPoint system and custom LabVIEW programming. All data was recorded and time-correlated. The setup allowed for control and monitoring of the test rig from an adjacent control room for operator safety. For this experiment, the AVL IndiCom system was configured to measure pressure inside the engine cylinder during operation using a Kistler type 6113B measuring spark plug. The Kistler spark plug and stock spark plug is shown in Figure 3.5. A copper spacer was added to the Kistler spark plug to allow for the proper depth into the combustion chamber. This limited however the number of threads available for screwing into the cylinder head. The Kistler pressure sensor can measure pressures from 0-20 MPa with an accuracy of less than ±0.5% within its operating temperature range of -20 °C to 350 °C. The crank angle signal was measured using a US Digital E6-1800-750-IE-D-H-DB optical encoder. The encoder measures crank angle to within ±0.1°. The AVL IndiCom data acquisition system utilizes high speed cylinder pressure and crank angle data to calculate the average indicated mean effective pressure and coefficient of variance over 400 engine cycles. These data were used to determine the engine's indicated power output.

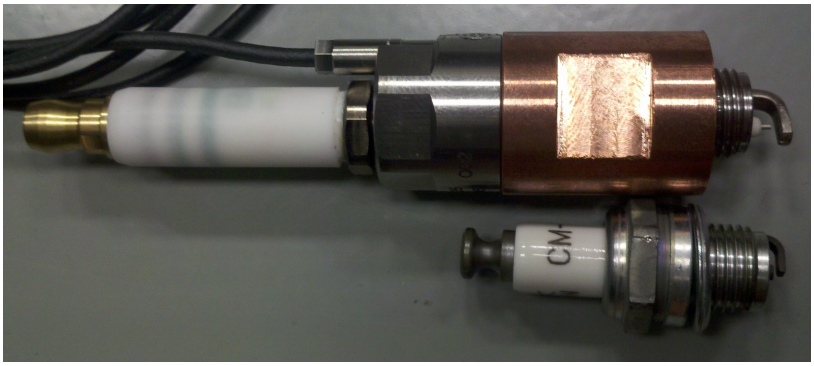

Figure 3.5: Kistler type 6113B measuring spark plug and stock spark plug

Table 3.2 is provided below as a summary of instrument uncertainties. The heat flux gauges used in one of the measurement techniques were custom fabrications that did not include accuracy information.

Table 3.2: Measurement Uncertainties

Measurement	Accuracy
Dynamometer Torque	± 0.5% of span
Engine Speed	± 0.5% of span
Intake Air Flow Meter	± 3% of reading
Fuel Flow Meter	± 2% of reading
Enclosure Air Flow Meter	± 2% of span
Temperature (intake)	± 1.5 °C
Temperature (exhaust)	± 0.4% of reading
In-Cylinder Pressure	± 0.5% of reading
Crank Angle	± 0.1°

3.2 Evaluated Measurement Techniques

This investigation aimed to quantify the heat rejection from the 55 cc single cylinder, gasoline-fueled, spark-ignition, two-stroke engine shown in Figure 3.1. Three measurement techniques were used to capture the thermal losses of the cylinder body. The first method indirectly measured the loss through an energy balance into and out of the system. The second method measured the enthalpy increase of air flowing past the outside of the cylinder body and cooling fins. The third method used heat flux gauges at three locations on the cylinder body.

3.2.1 Energy Balance Method.

Energy is brought into the engine system through the combustion of fuel and air and leaves through a variety of different mechanisms. Through the measurement of total energy into the system and measuring the different mechanisms for energy leaving, one can estimate the amount of energy lost through heat rejection. Heywood uses Figure 3.6 to show the flow paths of energy into and out of an engine [6].

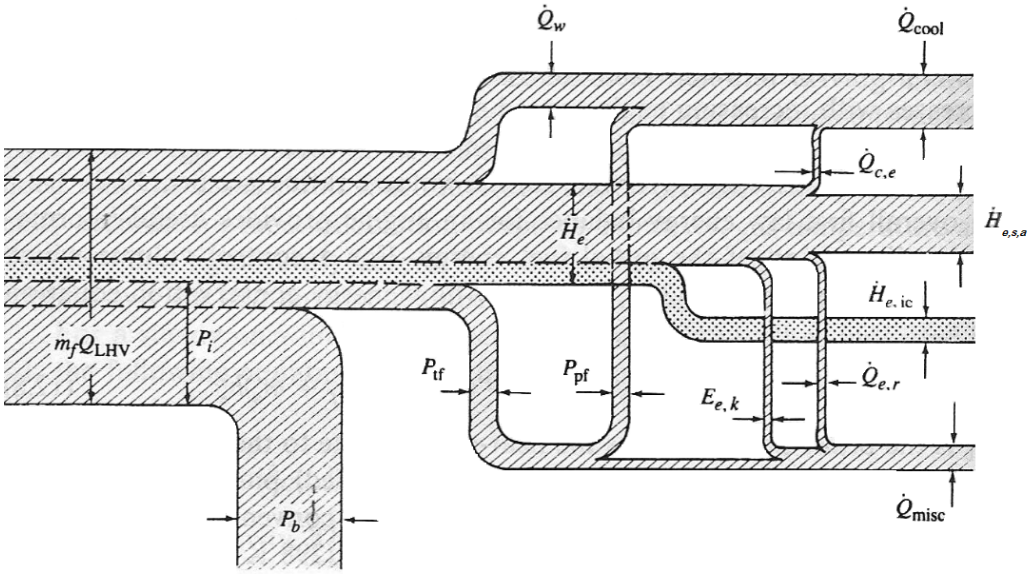

Figure 3.6: Energy flow diagram for an IC engine [6]

The resulting energy balance equation from Figure 3.6 is then:

$$\dot{m}_f Q_{\mathrm{LHV}} = P_b + \dot{Q}_{cool} + \dot{H}_{e,s,a} + \dot{H}_{e,ic} + \dot{Q}_{\mathrm{misc}} \tag{3.1}$$

The total fuel energy on the left ($\dot{m}_f Q_{\mathrm{LHV}}$) is balanced on the right by the sum of energy leaving as brake power (P_b), heat rejection ($\dot{Q}_{cool}$), exhaust enthalpy ($\dot{H}_{e,s,a}$), incomplete combustion ($\dot{H}_{e,ic}$), and miscellaneous thermal losses ($\dot{Q}_{\mathrm{misc}}$).

The ideal or maximum amount of this energy that can be used is calculated from the Otto efficiency in Equation 2.2, the fuel flow rate, and the lower heating value.

$$E_t = \eta_{th} \cdot \dot{m}_f \cdot Q_{\text{LHV}} \tag{3.2}$$

The ideal fuel conversion efficiency for the test engine was calculated using Equation 2.2. The geometric compression ratio was 10:1 as specified by the manufacturer. Using an average specific heat ratio of 1.35 and the geometric compression ratio, the ideal fuel conversion efficiency of this engine was 55.3%. To account for open ports during a portion of the stroke, the ideal fuel conversion efficiency was also calculated using the effective compression ratio. The exhaust port was the last air passage to be covered as the piston travels towards TDC. Measuring the length of the remaining stroke from the point of closure allowed for the swept volume of trapped air to be calculated. Dividing the combined volume of the measured swept volume plus the combustion chamber volume by the combustion chamber volume resulted in an effective compression ratio of 7.2:1. These measurements also allowed for a calculation of exhaust port closure as a function of crank angle. For the 3W-55i, exhaust port closure was found to be at 103° After Top Dead Center (ATDC). To further examine if a small amount of compression exists prior to exhaust port closure, the engine was motored (non-firing) while monitoring in-cylinder pressure. A view of in-cylinder pressure during the test is shown in Figure 3.7 as observed through the AVL IndiCom DAQ. The pressure is shown in units of bar as a function of crank angle. Effective compression ratio can then be calculated using Equation 3.3 assuming isentropic efficiency.

$$\frac{V_1}{V_2} = \frac{P_2}{P_1}^{\frac{1}{\gamma}} \tag{3.3}$$

The maximum in-cylinder pressure during the motoring test was 1650 kPa (16.5 bar) resulting in a calculated effective compression ratio of 7.4:1. With a 7.4:1 compression ratio, the ideal fuel conversion efficiency of the engine was 50.4%.

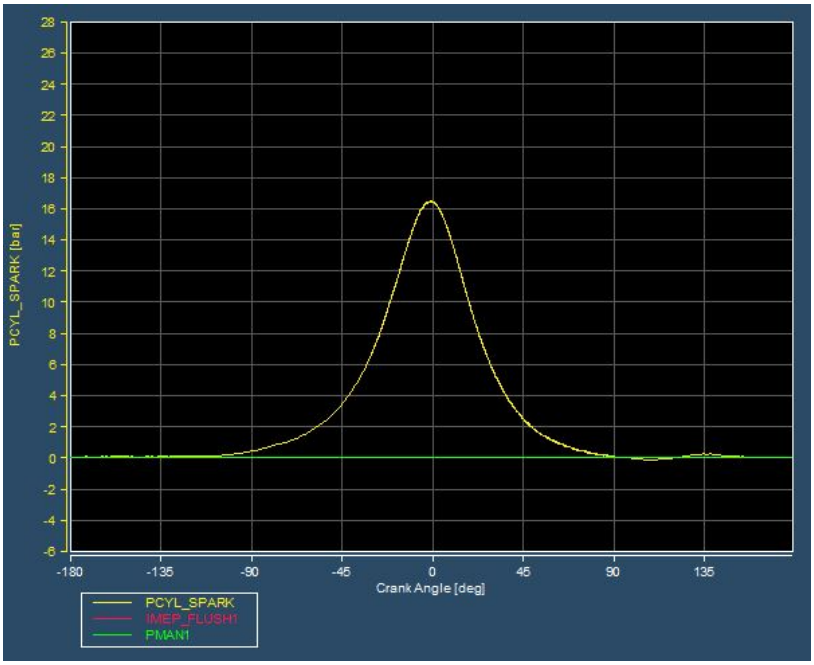

Figure 3.7: AVL pressure versus crank angle diagram during motoring (non-firing) cycle

The pressure trace during a firing cycle is shown in Figure 3.8. At approximately 105° Before Top Dead Center (BTDC) the pressure started to increase indicating exhaust port closure. The rate of pressure increase from 105° to 20° BTDC was the same as during the motoring test as expected. Around 20° BTDC the pressure trace during the firing cycle diverged from the trace of the non-firing cycle due to combustion. Spark timing is estimated at 10° prior to this point [7] at approximately 30° BTDC. Pressure peaked at approximately 7° ATDC. After the point of maximum pressure, the decreasing pressure corresponds to increasing cylinder volume as the piston travels towards BDC. There is a change in the rate of pressure decrease at approximately 105° ATDC. This indicates the opening of the exhaust port, symmetric to exhaust port closure at 105° BTDC.

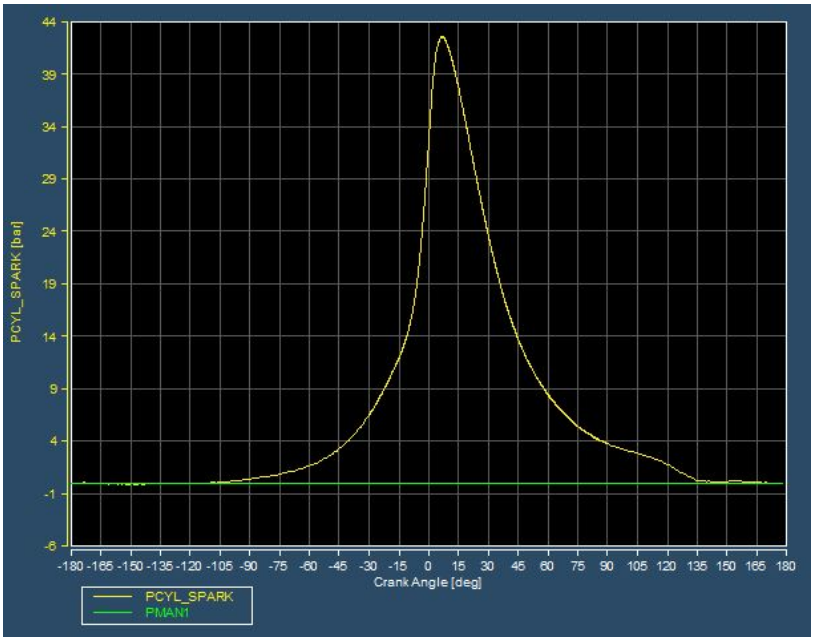

Figure 3.8: AVL pressure versus crank angle diagram during firing cycle

The Indicated Mean Effective Pressure (IMEP) obtained from the AVL IndiCom was used to measure the amount of power the engine produces before frictional and pumping losses. The indicated or IMEP-based power is then calculated by combining Equations 2.4 & 2.5.

$$P_i = \frac{\text{IMEP} \cdot N \cdot V_d}{n_c} \tag{3.4}$$

with N being the engine speed in revolutions per second, V_d is the engine displacement, and n_c is the number of revolutions per cycle (1 revolution per cycle for a 2-stroke).

The brake power is the amount of usable mechanical energy available at the point of measurement on the shaft. Brake power was calculated by measuring the torque (τ) at the dynamometer and multiplying by the angular speed.

$$P_b = \tau N 2\pi \tag{3.5}$$

The difference between the IMEP and Brake Mean Effective Pressure (BMEP) is the Friction Mean Effective Pressure (FMEP). FMEP accounts for the friction of internal

engine components, pumping losses, and in this research the friction of the drivetrain linking the engine shaft to the dynamometer. Pumping losses are minimized by operating at Wide Open Throttle (WOT) which minimizes air flow restrictions at the throttle plate.

3.2.2 Monitoring Heat Loss to External Engine Flow.

The second technique measured the amount of heat transferred to air that flowed past the cylinder body. An enclosure was built to contain the engine and measure the airflow ducted through. The engine intake air is routed to the carburetor separately and is not drawn from inside the enclosure. Similarly, the engine exhaust is routed out of the enclosure within a few centimeters to avoid interfering with the heat rejection measurements. This configuration of the test bench is shown in Figures 3.9 & 3.10 with a closer view of the backside in Figure 3.11.

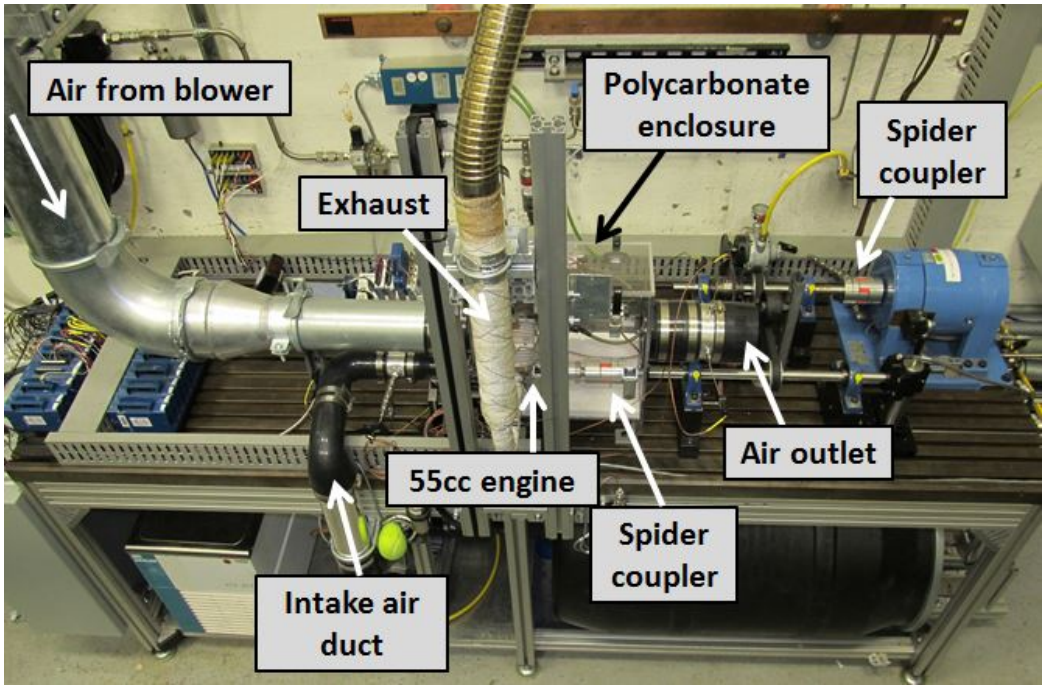

Figure 3.9: Overview of bench configured with ducted airflow through polycarbonate enclosure

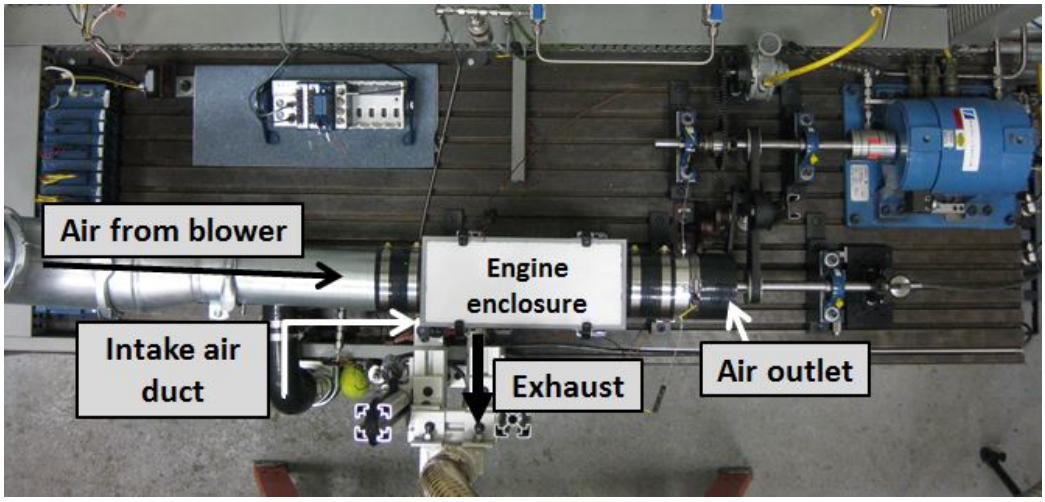

Figure 3.10: Top-down view of bench configured with ducted airflow through polycarbonate enclosure

The enclosure was constructed of a clear polycarbonate to allow for visual engine monitoring during tests. Air at a measured temperature and flow rate was then pumped into the container using the VFD and AC blower. Flow rates were representative of RPAs in flight with similar sized engines with a maximum of approximately 30.5 $\frac{\text{m}}{\text{s}}$ (100 $\frac{\text{ft}}{\text{s}}$). A foam gasket material was used at the seams of the enclosure to minimize air loss. The temperature of the airflow was then measured at the exit as an average of three thermocouples set up as a rake. This technique is similar to that used by Ajav with water as the working fluid [2]. The energy lost to the air is calculated by Equation 3.6.

$$\dot{Q} = \dot{m}_{\text{air}} c_p (T_{\text{out}} - T_{\text{in}}) \tag{3.6}$$

where $\dot{Q}$ is the heat transfer rate, $\dot{m}_{\text{air}}$ is the mass flow rate of the air into and out of the enclosure, and c_p is the specific heat of the working fluid. Radiative heat transfer effects were neglected because of the relatively low engine operating temperatures and the use of the polycarbonate enclosure.

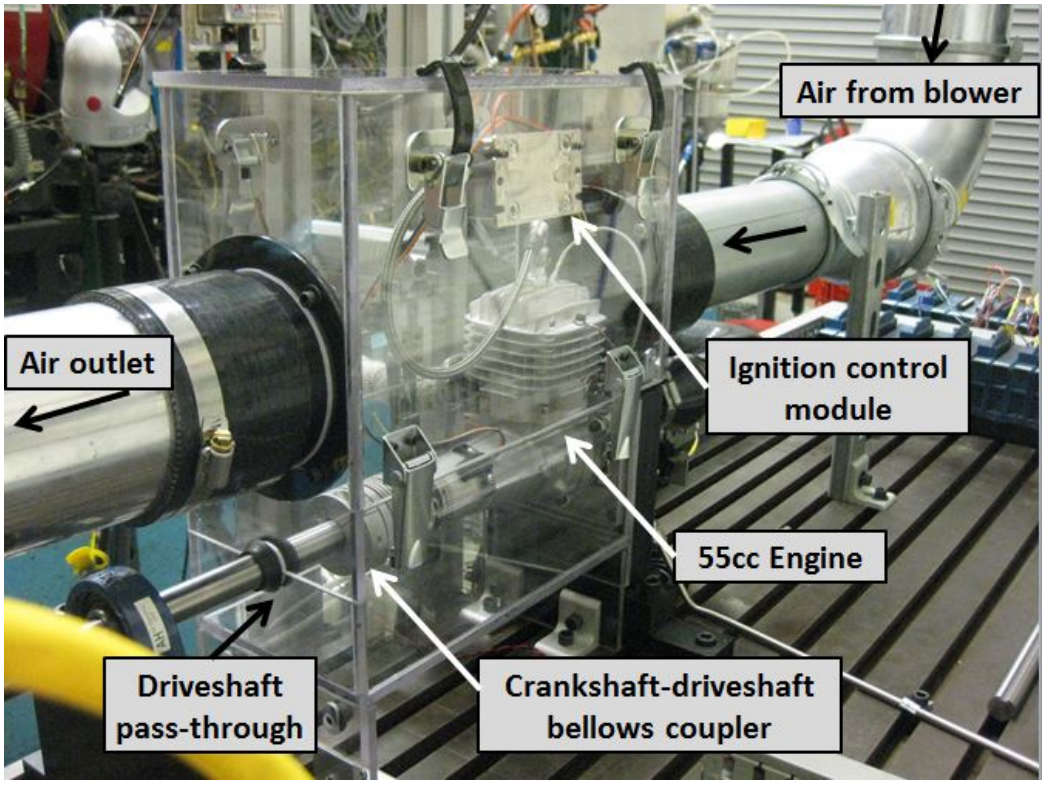

Figure 3.11: Engine within polycarbonate enclosure

The mass airflow was measured using an Omega FMA905A-V1 hot wire sensor inserted into the center of the duct upstream of the engine. An approximate ten diameters of duct was added upstream of the point of measurement along with five diameters downstream to accommodate flow profile development. The air speed was recorded with the DAQ as a linear 0-5 V output over the 0-50.8 $\frac{\text{m}}{\text{s}}$ range of the hot wire. Accuracy of the hot wire is reported at 1.5% of full scale and repeatability at ±0.2% of full scale. The mass airflow is then the product of the bulk velocity, duct cross-sectional area, and air density.

Insulation was added for a comparison measurements with and without enclosure insulation. The rigid-foam insulation was added to the inside of the enclosure as seen in Figure 3.12. The insulation was 1.9 cm ($\frac{3}{4}$ in) expanded polystyrene with a thermal conductivity of $k = 0.03\frac{\text{W}}{\text{mK}}$.

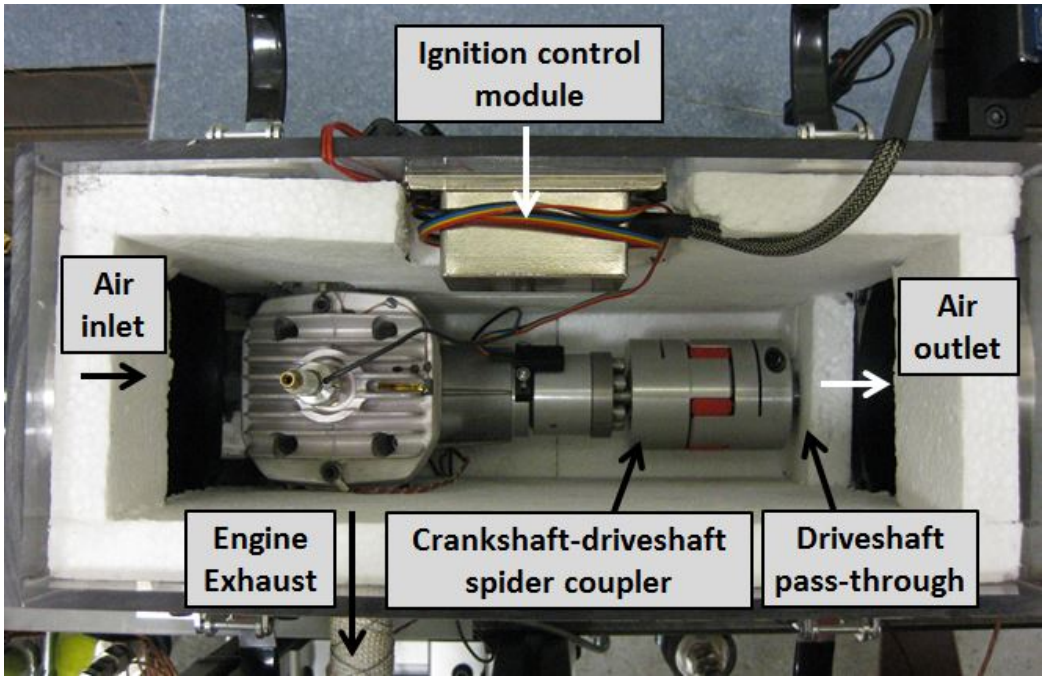

Figure 3.12: Engine within insulated polycarbonate enclosure

3.2.3 Heat-Flux Gauge Measurement.

Direct measurement of heat loss was accomplished by means of multilayer heat flux gauges. These heat flux gauges obtain a direct measurement of the heat flux by measuring the temperature difference between opposite sides of a thin layer of insulating substrate [4]. The frequency response of the gauge is increased as the thickness of the insulator is reduced. The gauge consisted of an upper and lower temperature-dependent platinum resistor similar to a Resistance Temperature Detector (RTD). The change in resistance with temperature of the platinum is nearly linear. The temperature at each resistor element is calculated using

$$T = \frac{R_0 - R}{\alpha_R \cdot R_0} \tag{3.7}$$

where R is the measured resistance at temperature, R_0 is the element resistance at a calibration temperature, α_R is the temperature coefficient determined through calibration (Table 4.2), and T is the measured temperature. A National Instruments 9217 24-Bit analog

input module was used with internal excitation and Wheatstone bridge to capture the small changes in resistance as the temperature changed. Current values running through the bridge must be kept small to avoid heating the gauge element thus affecting the temperature and heat flux measurement. Once the temperature of the upper and lower elements are measured, the heat flux ($\frac{\text{kW}}{\text{m}^2}$) can then be calculated.

$$Q" = -k\frac{(T_{\text{upper}} - T_{\text{lower}})}{dx} \tag{3.8}$$

The two elements are separated by Kapton with a conductivity of $k = 0.179\ \frac{\text{W}}{\text{m-K}}$ and a thickness of $dx = 51.1\mu\text{m}$. The total energy the cylinder gives off as heat rejection is then the heat flux multiplied by the exterior surface area of the cylinder head. Due to the inability to cover the entire cylinder body with heat flux gauges, the accuracy of this method is limited. Energy loss calculations for this method used the heat flux values at each of the three gauge locations. The surface area was measured to be approximately 640 cm^2.

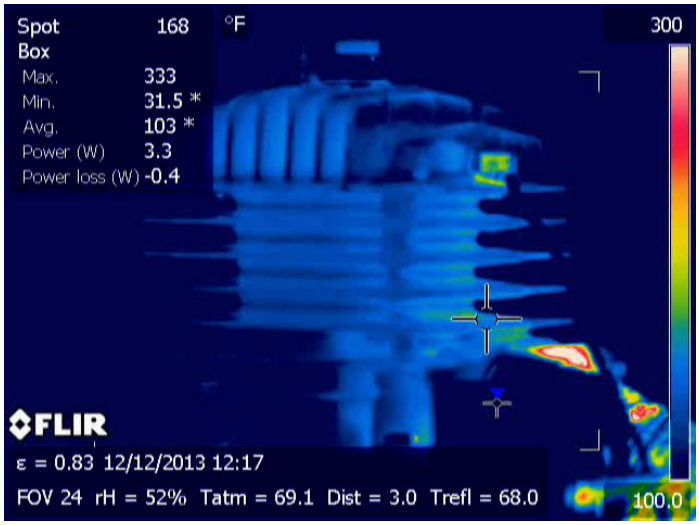

Figure 3.13: IR image of intake side used in evaluating temperature distribution

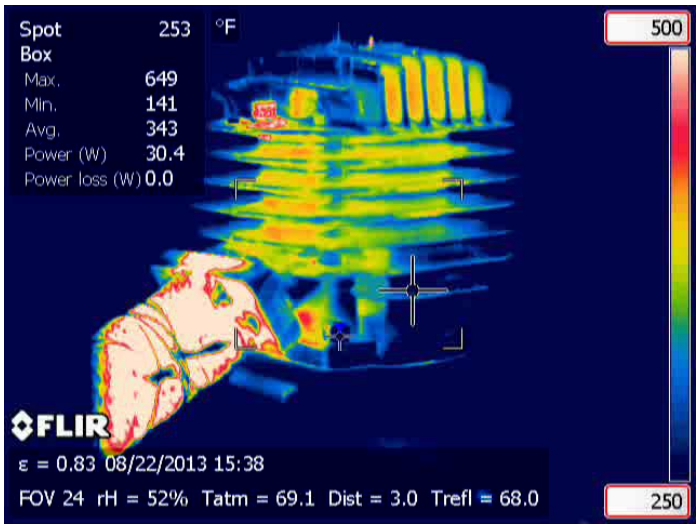

Figure 3.14: IR image of crankshaft side used in evaluating temperature distribution

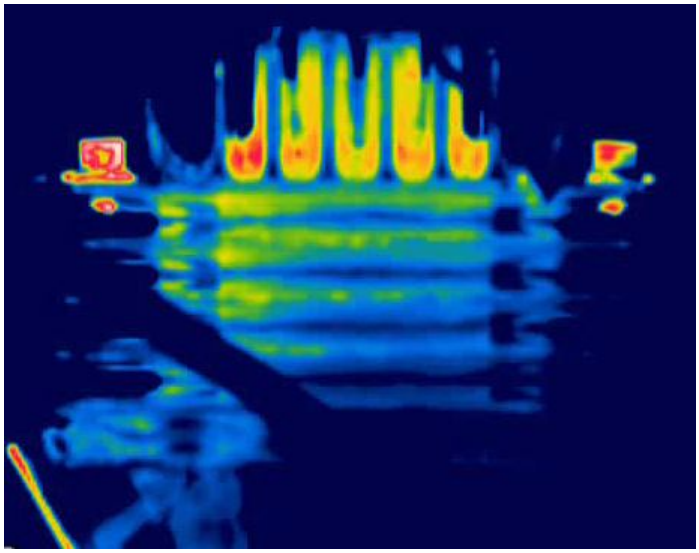

Figure 3.15: IR image of crankshaft side showing increased temperatures at top left (exhaust side)

To aid in the placement of the heat flux gauges, a FLIR SC640 Infrared (IR) camera was used to gather a continuous mapping of engine temperatures within the camera's field of view. This enabled the sensors to be strategically and non-invasively placed around the cylinder head at locations that would be representative of the cylinder body temperature. The IR camera also proved helpful in evaluating the temperature distribution on the cylinder head. The IR images in Figures 3.13-3.15 show the cylinder body temperatures during operation. Based on these and additional images, heat flux gauges were placed between fins on the cylinder body at three locations as shown in Figures 3.16 & 3.17. The first gauge was placed on the side facing the airflow, a second was placed on the side facing away from the airflow, and a third was placed at the top of the cylinder. Embedded E-type thermocouples were used to gather reference temperatures needed to calibrate the thermal IR images.

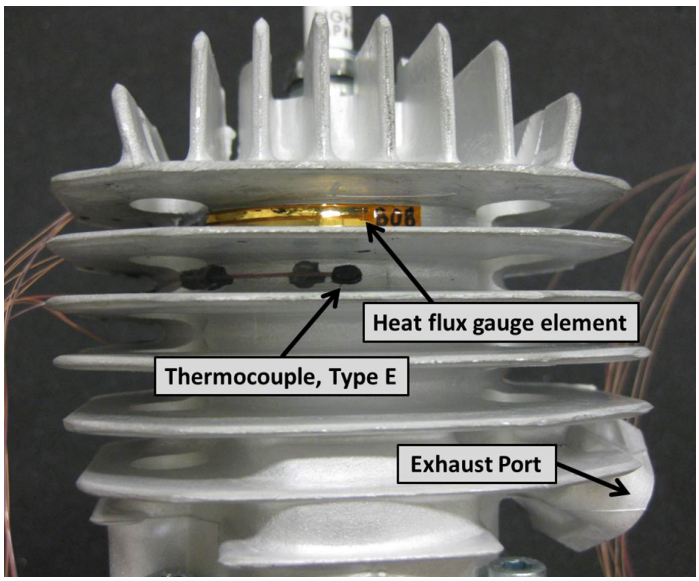

Figure 3.16: Thin-film heat flux gauge and thermocouple placement facing airflow

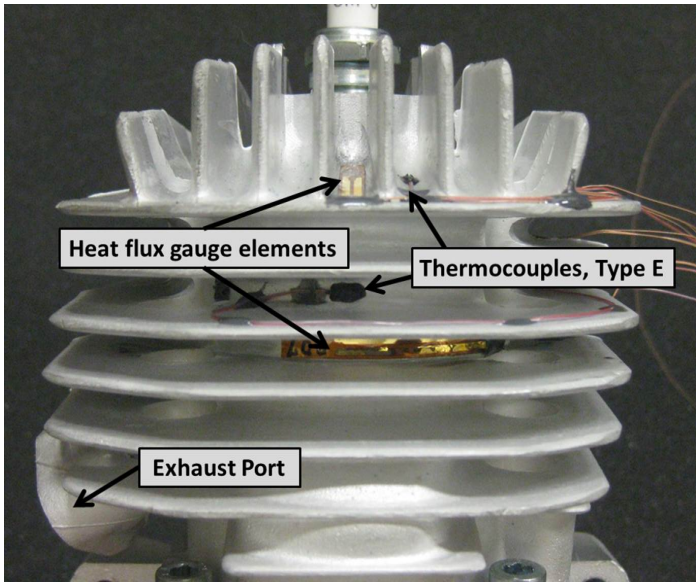

Figure 3.17: Second and third thin-film heat flux gauges and thermocouples, placed on side opposite the airflow

IV. Results and Analysis

The objectives of this research effort were to evaluate engine heat rejection measurement techniques and to use the techniques to characterize the thermal loss in a small RPA engine. This chapter provides an analysis of results from the three heat rejection measurement techniques described in the previous chapter. The chapter starts with an overview of the engines that were tested and how they performed and then moves into results from the three measurement techniques. The energy balance was the first measurement method used and provided an initial estimate of the heat rejected from the cylinder body along with an analysis of engine performance. The second method measured the enthalpy increase of air flowing past the external cylinder body. This measurement used the polycarbonate enclosure and provided a direct measurement of the heat rejected. The third method utilized the heat flux gauges to measure the heat flux at three locations on the cylinder body. Estimates of total heat loss were then calculated based on these heat flux measurements and the total surface area of the cylinder body. The chapter closes with a discussion comparing the accuracy and practicality of the three methods.

For each measurement method, measurements were taken with the engine running from 4000 rpm up to 7900 rpm. This is the range at which the engine could consistently operate without misfires. Engine speed is converted from revolutions per minute into mean piston speed, $\bar{S}_p$ in Equation 4.1. Mean piston speed is a common engine speed parameter used in comparing engines of different sizes. A conversion between rpm and mean piston speed for the range of test points is provided in Table 4.1. At each speed, measurements were taken at throttle settings that provided maximum brake power (100%), 75%, 50%, and 25% power.

$$\bar{S}_p = 2 \cdot \text{Stroke} \cdot N \tag{4.1}$$

Table 4.1: 3W-55i engine speed conversion

Engine Speed, N (rpm)	4000	4500	5000	5500	6000	6500	7000	7500	7900
Mean Piston Speed, $\bar{S}_p$ ($\frac{\text{m}}{\text{s}}$)	4.7	5.3	5.8	6.4	7.0	7.6	8.2	8.8	9.2

4.1 Test Engines

Each test matrix of a full speed and throttle sweep was run three times on each of three 3W-55i engines. Engine #1 was used during the initial setup of the small engine test bench. The engine was run with the Kistler pressure transducer spark plug and the smaller DC-powered cooling blower. Testing of this engine ended with the ejection of the Kistler spark plug from the cylinder head. Disassembly of Engine #1 revealed severe scoring on the piston and cylinder walls. The cause of the spark plug failure and engine damage was investigated. Records indicated that oil had always been present in the fuel mixture, thus eliminating the lack of oil as a cause. The amount of two-stroke oil in the fuel was at ratios consistent with manufacturer recommendations (1:32 during break-in, 1:100 after break-in). The cause of the engine damage was attributed to insufficient cooling resulting in elevated operating temperatures. The ejection of the spark plug was likely due to a combination of factors leading to the loosening of the spark plug over several test runs. Some of these factors include installing the spark plug without a torque wrench, engine vibration, fewer threads on the Kistler spark plug versus the stock plug (Figure 3.5), and thermal cycles of engine operation and cooling. This engine was found to produce the least brake power of the three engines. Decreased brake power values were consistent with increased friction power when compared to the other two engines.

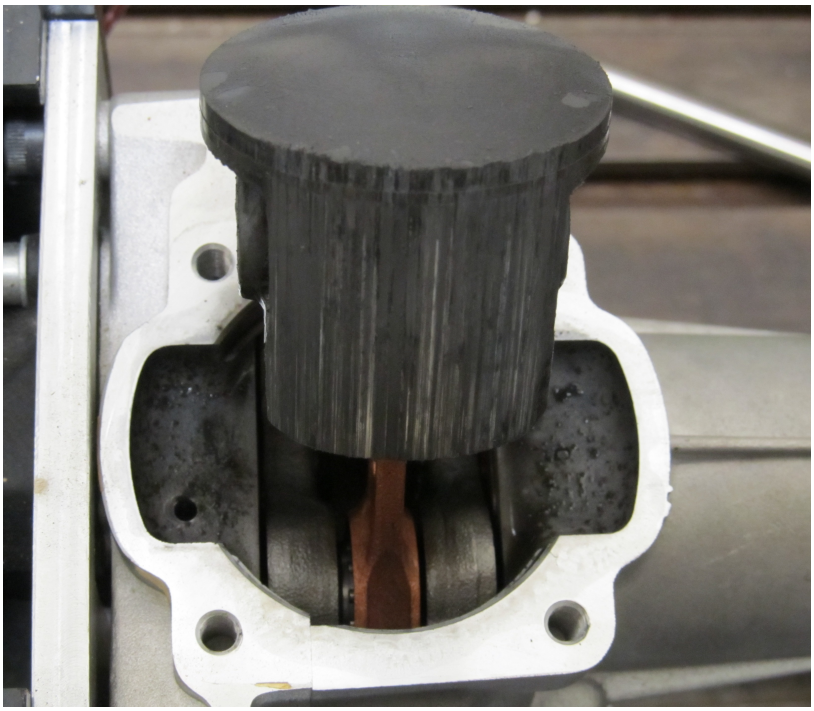

Figure 4.1: Piston scoring of 3W-55i Engine #1

Engine #2 was modified with the addition of a flush-mount pressure transducer. A port was drilled into the top of the cylinder head as seen in Figure 4.2. This allowed for a pressure transducer to be added next to the spark plug. A comparison of the two pressure measurements and corresponding engine performance is being done in a separate effort by AFRL. This engine performed the three test runs without failure. This engine was also disassembled after completion of testing. No signs of scoring were present, however there was a darkened area on the exhaust port side of the combustion chamber as seen in Figure 4.3. The specific cause of this marking is unknown.

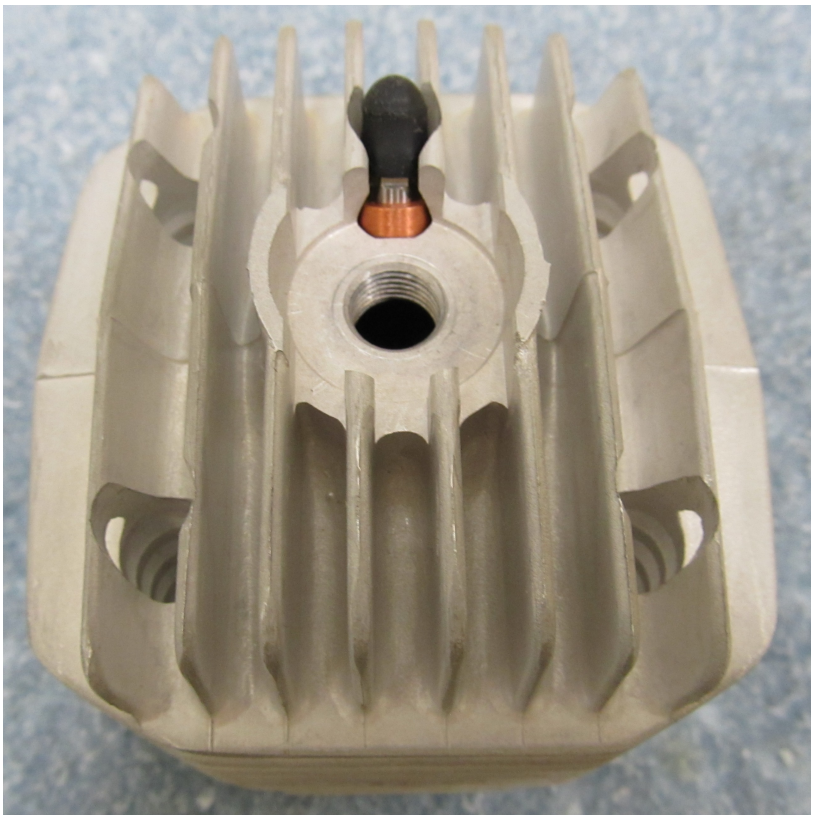

Figure 4.2: 3W-55i Engine #2 with flush mount pressure transducer port

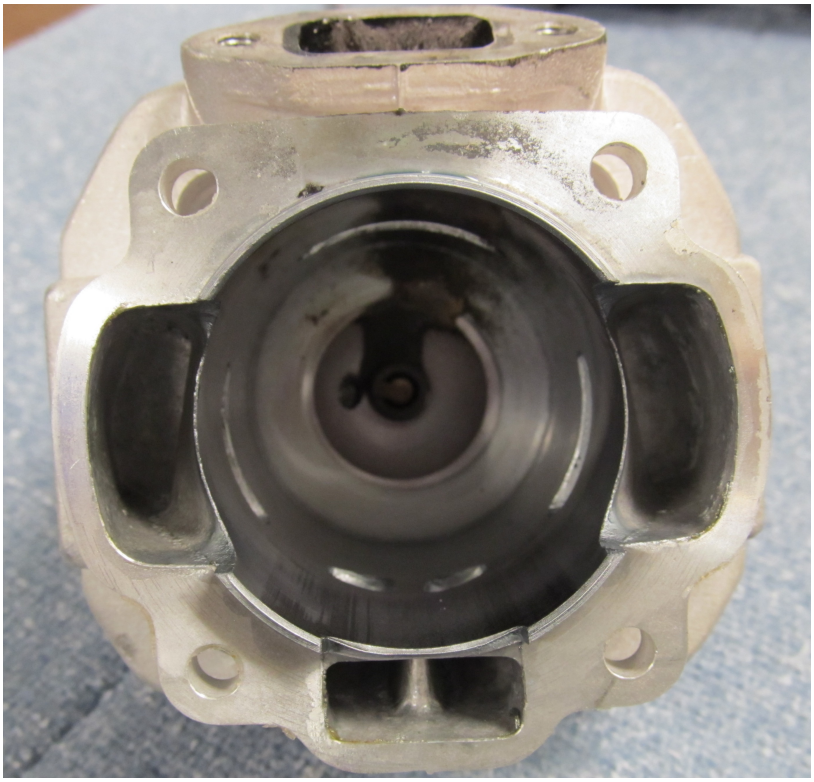

Figure 4.3: Combustion chamber marking of 3W-55i Engine #2 with Kistler spark plug installed

Engine #3 was instrumented with the three thin-film heat flux gauges and Type-E thermocouples. This engine shown in Figure 4.4 also performed the three test runs without failure. All three measurement techniques were used simultaneously on Engine #3 allowing for a direct comparison between methods. The data from Engine #3 was the primary focus of the results analysis. This engine could not be disassembled for inspection and photos because of ongoing testing with other research efforts.

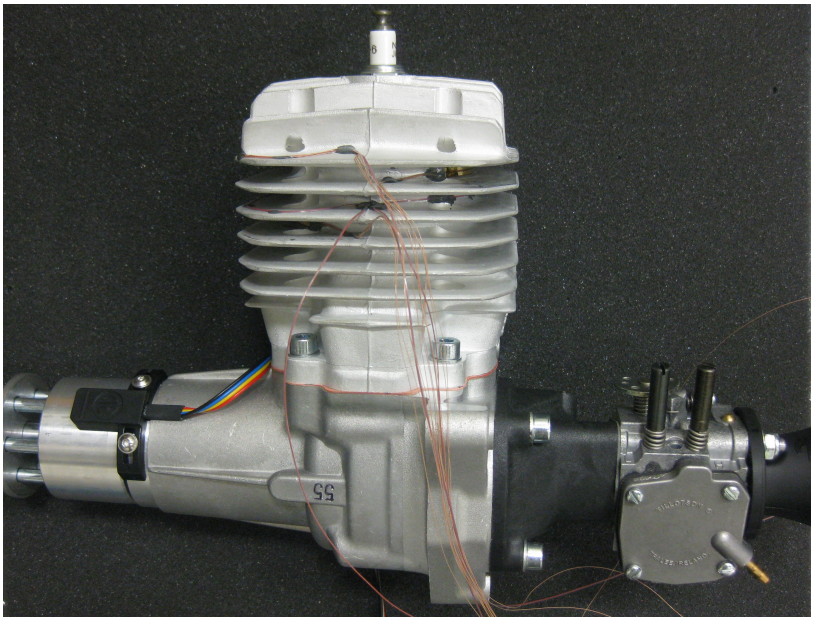

Figure 4.4: 3W-55i Engine #3 with heat flux gauges and thermocouples installed

The throttle position for each power value was determined prior to the test runs by running the engine at 6000 rpm and doing a throttle sweep from idle to WOT. These throttle sweeps are shown in Figure 4.5 as a function of the LabVIEW setting for the throttle servo motors.

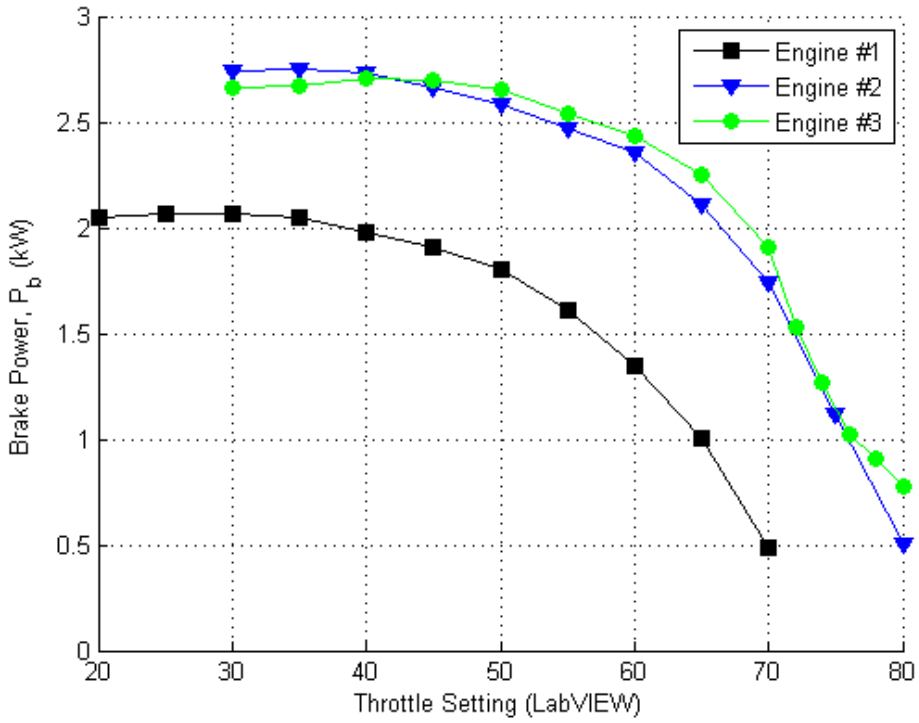

Figure 4.5: Throttle sweeps for Engines #1-3 at 6000 rpm

All three engines were checked for smooth operation prior to running the heat rejection test methods. The carburetor low and high adjustment screws were screwed in (leaned) or out (enrich) as needed to bring the air/fuel mixture closer to stoichiometric conditions. Stoichiometric conditions or rather slightly lean at an equivalence ratio of 1.05 was the indicator of where the engine should produce maximum power. Proper tuning to a near stoichiometric mixture was done through the observation of engine sound, the exhaust wide-band O_2 sensor, and a real-time LabVIEW calculation of the equivalence ratio.

$$\phi = \frac{\frac{m_{air}}{m_{fuel}}}{(\frac{m_{air}}{m_{fuel}})_{st}} \tag{4.2}$$

Prior to testing, the mixture from the carburetor in Engine #1 was found to be too rich. A second airflow meter was installed to minimize airflow restrictions before tuning was performed through the adjustment screws. Engine #2 ran smoothly without excessive

misfires with the factory carburetor settings and was not adjusted. Engine #3 was found to be too rich prior to the test runs. The carburetor screws were adjusted and the equivalence ratio values ended up slightly below that of Engine #2. A plot of the equivalence ratios as tested for all three engines is shown in Figure 4.6. Test Runs #1 and #2 of Engine #1 are not represented in the plot due to difficulty during setup in recording the correct airflow. The values plotted for Engines #2 & #3 are averaged from the three test runs.

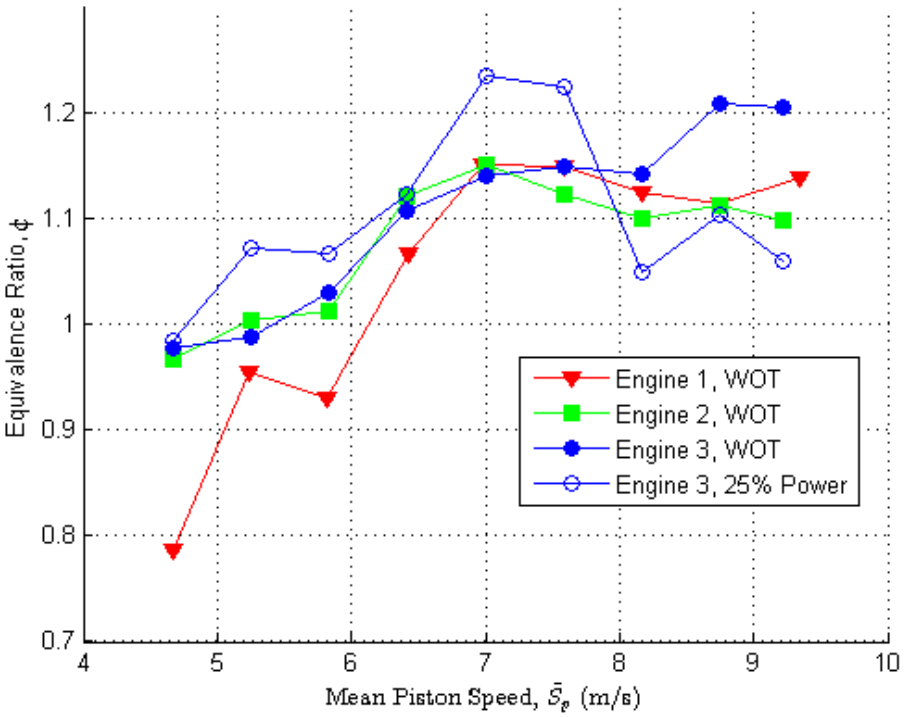

Figure 4.6: Equivalence ratio, ϕ, of Engines #1-3

There is a trend that the mixture becomes richer with engine speed for Engine #3. The capability to tune for proper mixture under all speed and throttle settings is limited with the use of a simple carburetor. For more refined mixtures under all load conditions

a fuel injection system would need to be added. This is one area identified for future improvements and further testing.

4.2 Energy Balance Results

This section documents the results from performing a balance on the energy entering and leaving the engine during operation. The fuel flow rate of a PRF with a known Lower Heating Value (LHV) provides an accounting for energy entering the engine. The method then consists of accounting for the mechanisms through which energy can leave the engine.

4.2.1 Energy Entering Engine.

The energy entering the engine was calculated using the measured fuel flow rate and the LHV of the PRF fuel. Fuel flow rates were measured at each loading condition and ranged from 11-42 $\frac{\text{mL}}{\text{min}}$. These rates were then converted to a mass flow rate using a temperature adjusted density of the fuel. The nominal density value was 702 $\frac{\text{g}}{\text{L}}$ resulting in fuel mass flow rates of 0.13-0.53 $\frac{\text{g}}{\text{s}}$. The fuel mass flow rate at each point can then be multiplied by the LHV of the fuel. The fuel used was a 98-octane rated PRF blend of 98% isooctane (LHV = 44.791 $\frac{\text{MJ}}{\text{kg}}$), 2% n-heptane (LHV = 44.926 $\frac{\text{MJ}}{\text{kg}}$) [17]. Synthetic 2-stroke engine oil was then added at a ratio of 1:100 of the octane-heptane blend. The resulting LHV of the blended fuel was 44.794 $\frac{\text{MJ}}{\text{kg}}$. Figure 4.7 shows the resulting total fuel energy entering the engines at full power (WOT) and 25% power. These values are averaged between the three runs for each engine. Data at 25% power was not intially tested and is therefore unavailable for Engine #1.

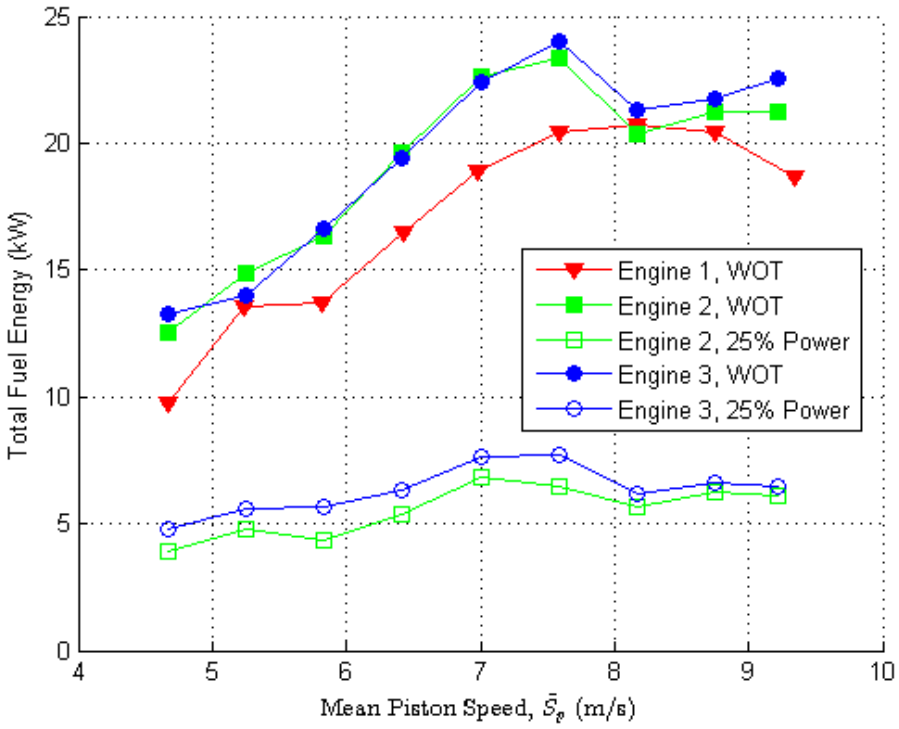

Figure 4.7: Total fuel energy of Engines #1-3 at full and 25% power settings

The incoming fuel energy in Figure 4.7 increases with engine speed except for a 0.3 kW decrease at WOT when the engine operates at 7000 rpm (8.2 $\frac{\text{m}}{\text{s}}$ mean piston speed, $\bar{S}_p$). This is a point of decreased fuel flow since the only variable in the plot is fuel flow. The cause of the decreased fuel flow was initially thought to be the tuning of the two-needle carburetor. To further investigate, the air flow over the same loading conditions was plotted in Figure 4.8. The airflow in this region is also decreased. Decreased airflow through the carburetor will result in less fuel being introduced into the charge. The carburetor cannot be tuned to allow for increased airflow. This decrease in airflow is attributed to gas exchange dynamics while at this loading condition.

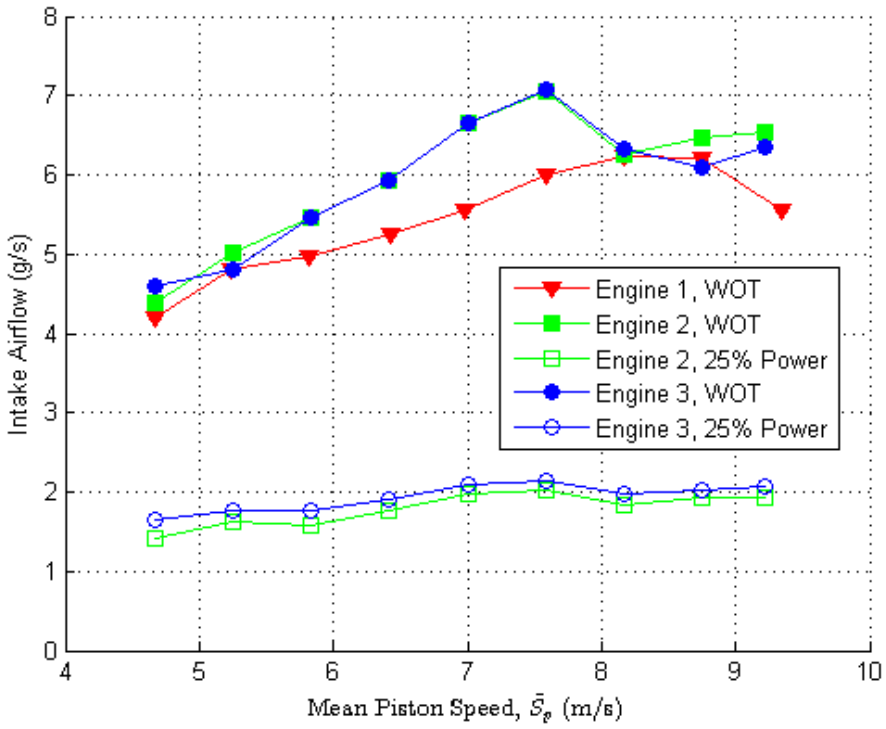

Figure 4.8: Air mass flow rates of Engines #1-3 at full and 25% power settings

4.2.2 Energy Exiting Engine.

The avenues for energy to leave the engine are as power, total exhaust enthalpy, unburned fuel, and thermal energy given off at the cylinder body. These energy flow paths were previously shown in Figure 3.6. A rough estimate in automotive applications assumes approximately 30% for power, 30% for exhaust enthalpy, and another 30% for heat rejection. Both brake and indicated power values were measured with each test. Brake power was measured with the dynamometer. Indicated power was calculated with the IMEP obtained with the in-cylinder pressure transducer and AVL IndiCom combustion analyzer. Exhaust enthalpy was calculated as the product of the intake air mass flow rate, an average specific heat ($c_p = 1.005 \frac{\text{kJ}}{\text{kg-K}}$), and the difference in temperature between the air entering

the carburetor and the air exiting the exhaust port. The remaining mechanism for energy to leave the system is as thermal energy from the cylinder body and is the primary focus of this effort. Although the heat rejected from the cylinder is not directly measured in this method, an estimate is obtained by subtracting the power and exhaust enthalpy from the total fuel energy.

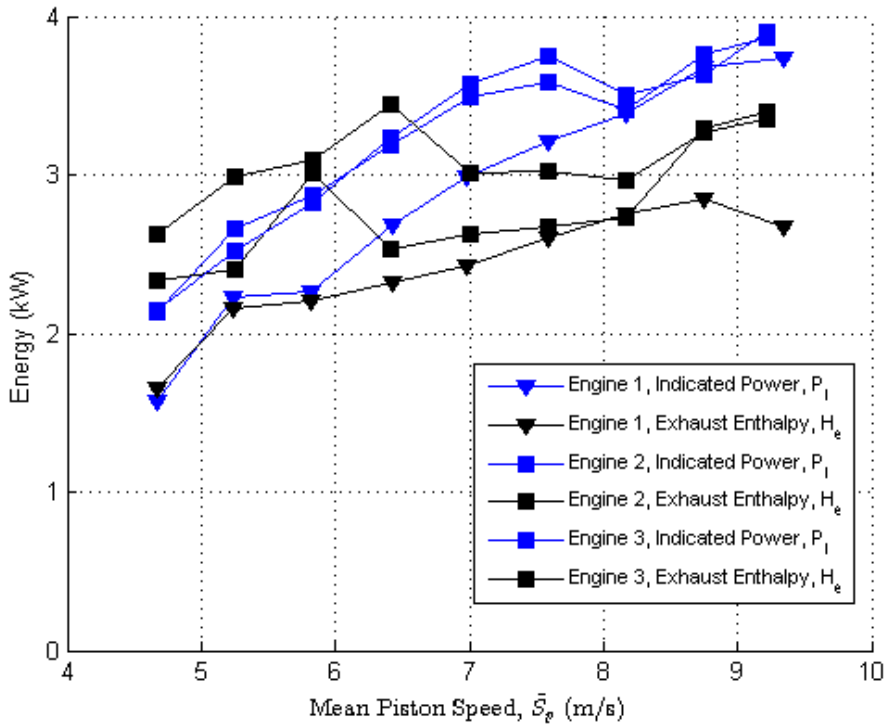

Figure 4.9: Indicated power and exhaust enthalpy of Engines #1-3 at WOT

The indicated power and exhaust enthalpy values are plotted in Figure 4.9 for all three engines at WOT. The indicated power output of Engines #2 and #3 are seen to be similar and values from Engine #1 are lower. Exhaust enthalpy increases with increased engine speed to a maximum of 4.0 kW at 7.6 $\frac{\text{m}}{\text{s}}$ (6500 rpm).

A comparison of power values from all three engines is shown in Figure 4.10. The values shown are an average from the three test runs for each engine. The plot includes indicated, brake and friction power. The difference between the indicated power and brake power is the friction power. As discussed earlier, this friction is a summation of engine friction, pumping losses, and drivetrain friction. The higher friction power seen in Engine #1 corresponds to the cylinder scoring and thus increased internal engine friction. For the remainder of the analysis methods, the data from Engine #1 will be ignored due to the low power and increased friction values.

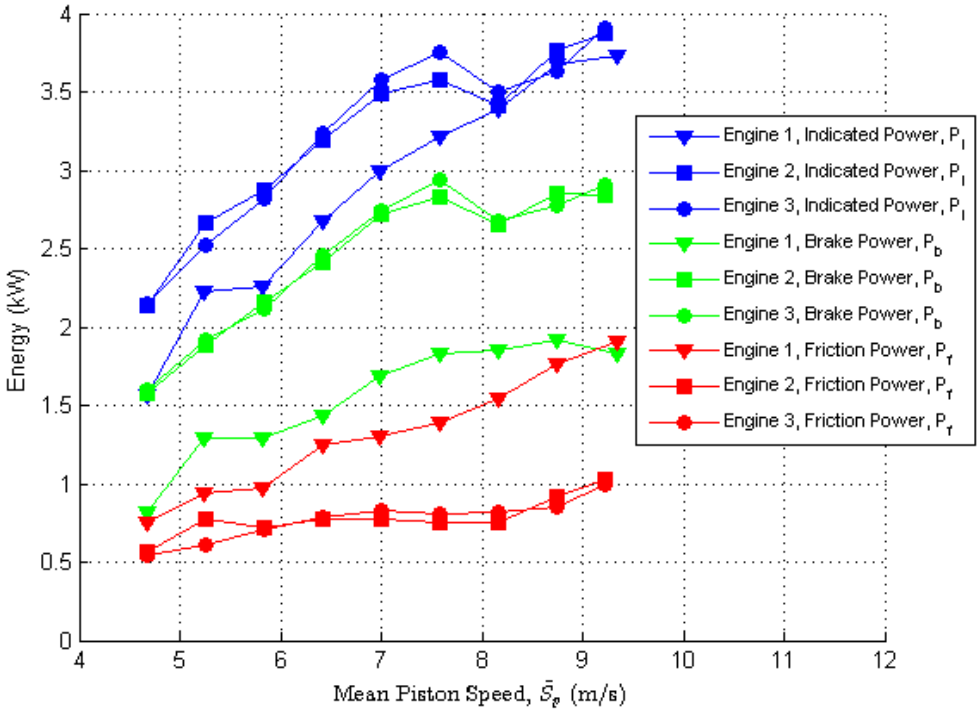

Figure 4.10: Comparison of power curves of Engines #1-3 at WOT

Examining the values for Engine #3 in Figure 4.10 shows maximum indicated power was 3.9 kW and maximum brake power was 2.9 kW, both at 9.2 $\frac{m}{s}$ (7900 rpm). Total friction power increased only slightly with speed from 0.5 kW at 4.7 $\frac{m}{s}$ to 1.0 kW at 9.2 $\frac{m}{s}$.

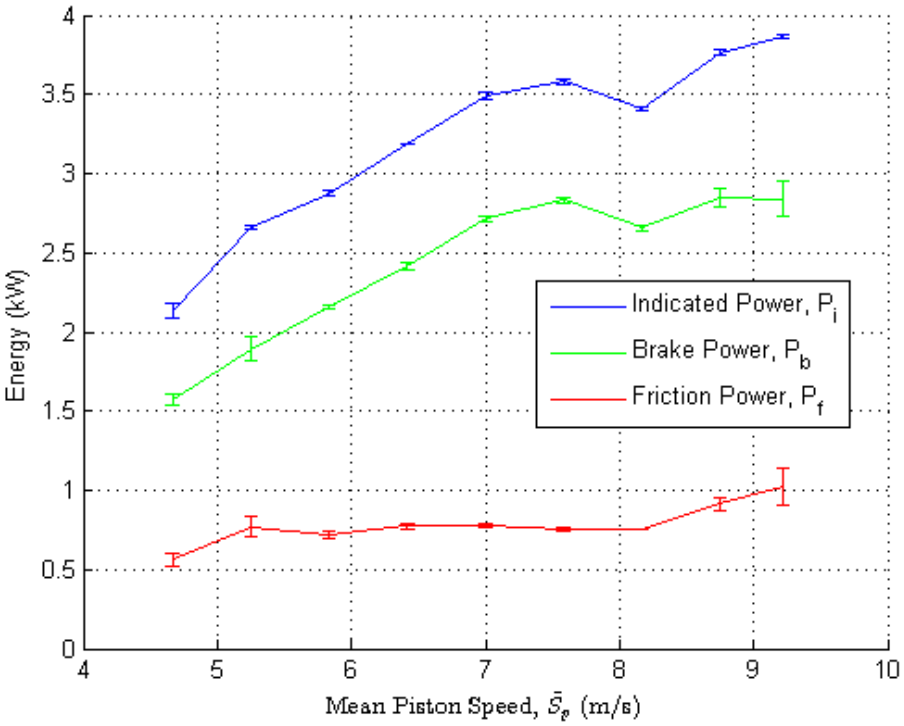

Figure 4.11: Power and energy values of Engine #2 at WOT

The average power values of the three runs of Engine #2 are shown in Figure 4.11. Similarly, the average power values during the three runs of Engine #3 are shown in Figure 4.12. Error bars have been added to show the standard deviation of each of the points between the three runs. There is only slight variation between the runs of Engine #2 and also between the runs of Engine #3.

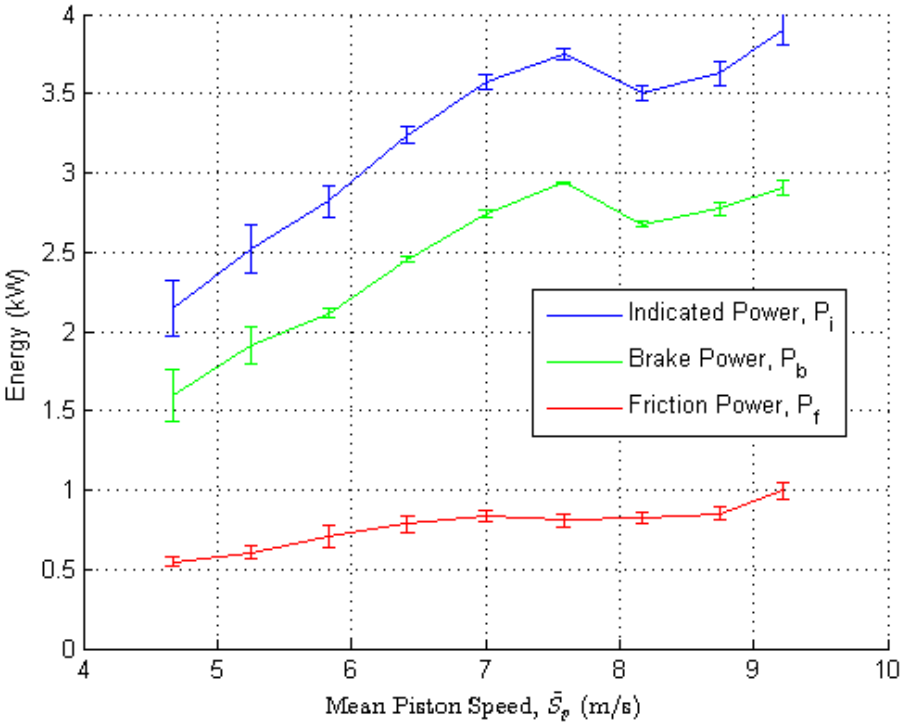

Figure 4.12: Power and energy values of Engine #3 at WOT

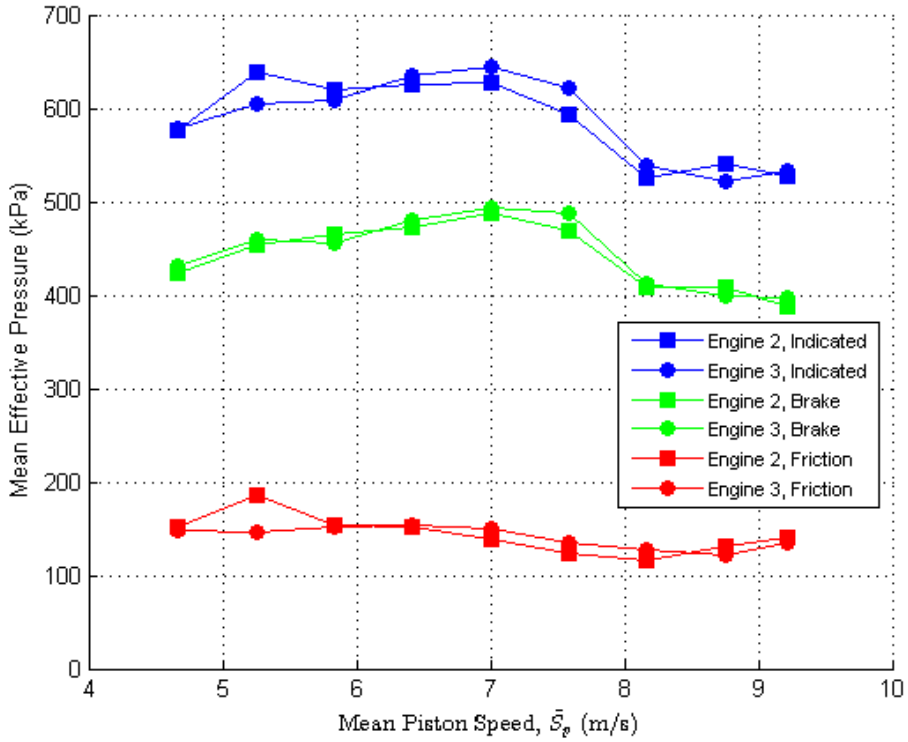

Figure 4.13: Mean effective pressures of Engines #2 and #3 at WOT

The previously mentioned power values were also converted into mean effective pressure values

$$\text{MEP} = \frac{P}{V_d \cdot N} \tag{4.3}$$

where V_d is the displacement volume. These mean effective pressures are shown in Figure 4.13 and allow for a non-dimensionalized comparison to engines of varying sizes.

Additionally, for comparison purposes BSFC is shown in Figure 4.14 for Engines #2 and #3. Included in the plot is data from a 95 cc Brison two-stroke engine with a port fuel-injected modification [8]. BSFC is the ratio of fuel consumption to brake power.

$$\text{BSFC} = \frac{\dot{m}_f}{P_b} \tag{4.4}$$

At WOT, all three engines measured approximately the same BSFC at 600-700 $\frac{\text{g}}{\text{kW-h}}$. At the 25% power setting, Engine #3 has increased BSFC which corresponds with the high equivalence ratios measured at this power setting.

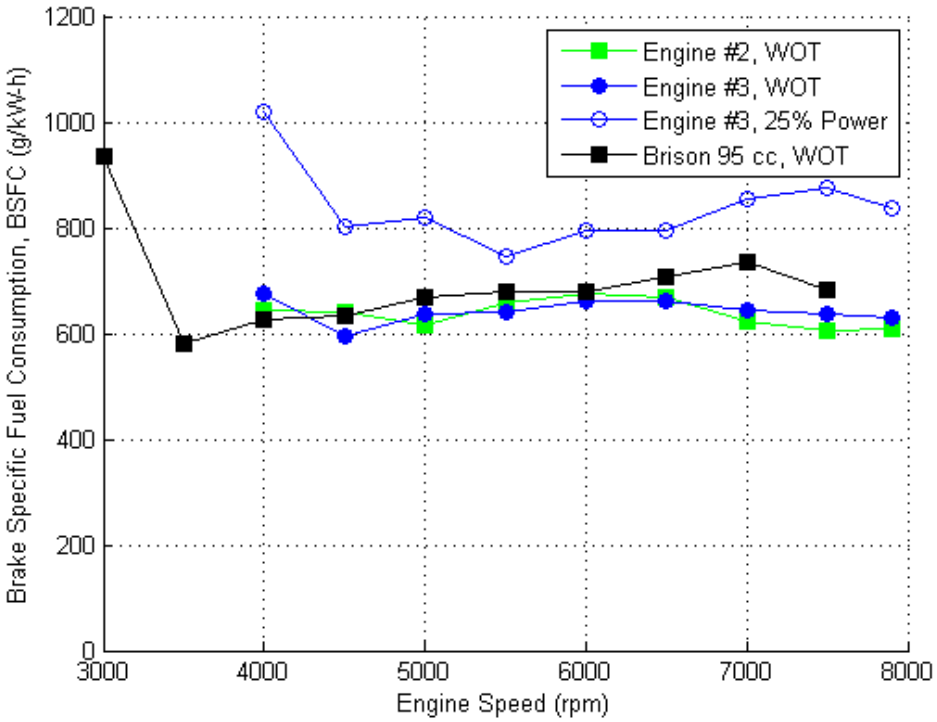

Figure 4.14: Brake Specific Fuel Consumption of Engines #2 and #3 and a 95 cc Brison

4.2.3 Energy Balance Analysis.

The energy entering the engine and the measured paths of energy leaving the engine combine to form the components of the energy balance. The energy balance equation used was:

$$\dot{m}_f Q_{\text{LHV}} \approx P_i + \dot{Q}_{cool} + \dot{H}_e + \dot{H}_{e,ic} + \dot{H}_{e,sc} \tag{4.5}$$

This equation is modified slightly from Equation 3.1. A term is added to account for the short-circuiting losses ($\dot{H}_{e,sc}$) found in two-stroke engines. The power term is switched from brake power to indicated power (P_i) to exclude the energy lost as friction in the drivetrain. A final change is dropping the miscellaneous thermal loss term ($\dot{Q}_{misc.}$) as radiation is neglected. Radiation is neglected due to low engine temperatures and operating within the polycarbonate enclosure. The final equation used to approximate the heat rejection is then:

$$\dot{Q}_{cool} \approx \dot{m}_f Q_{\mathrm{LHV}} - P_i - \dot{H}_{e,s,a} - \dot{H}_{e,ic} - \dot{H}_{e,sc} \tag{4.6}$$

Engine #3 is the focus for the remainder of the presented results. Again, Engine #3 is the focus of the results analysis because it was the only engine where all three measurement techniques were used. Data from the three test runs of Engine #3 were averaged and the following results are plotted as the averaged values.

Figure 4.15 shows the averaged runs from Engine #3 with the measured amounts of energy entering and leaving the engine. A sum of indicated power and exhaust enthalpy does not equal the total fuel energy. The difference is made up of short-circuiting, incomplete combustion, and the thermal energy rejected as heat at the cylinder body.

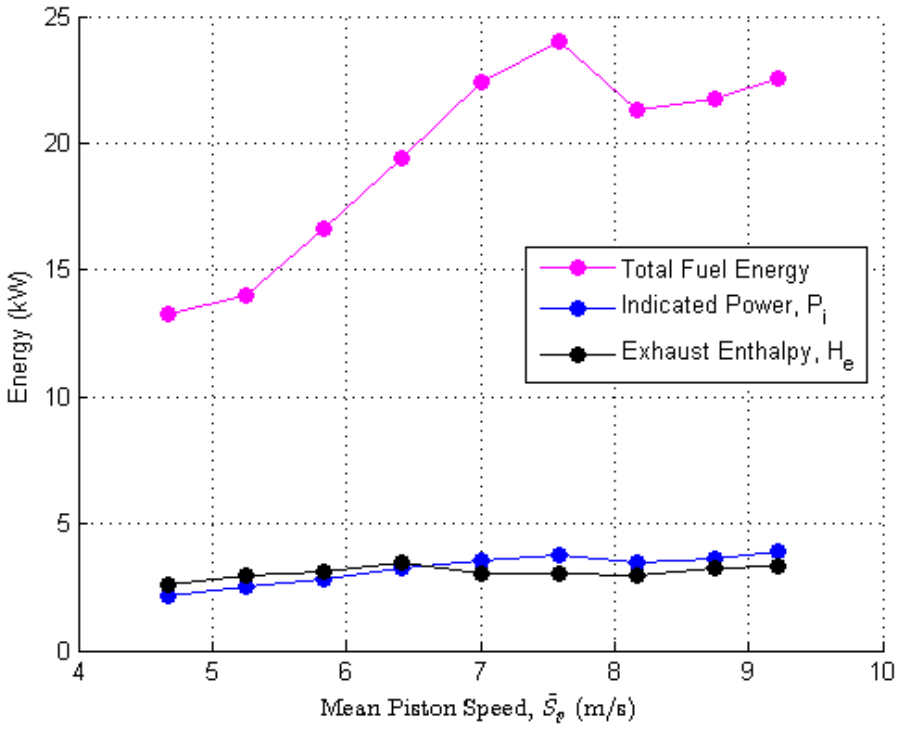

Figure 4.15: Total fuel energy, indicated power, and exhaust enthalpy flux of Engine #3 at WOT

Fuel conversion efficiency was determined using Equation 2.1. An evaluation of Engine #3 power values as a percent of total energy is plotted over the speed range in Figure 4.16. The blue line is the indicated power efficiency with a maximum of 18.0% at 5.3 $\frac{\text{m}}{\text{s}}$ (4500 rpm). Maximum brake power efficiency in green was 13.7% also at 5.3 $\frac{\text{m}}{\text{s}}$. The combined friction of the internal engine components, engine components, and pumping power remained relatively constant at approximately 4% of the fuel energy. Exhaust enthalpy decreased with engine speed ranging from 13-21% of the fuel energy.

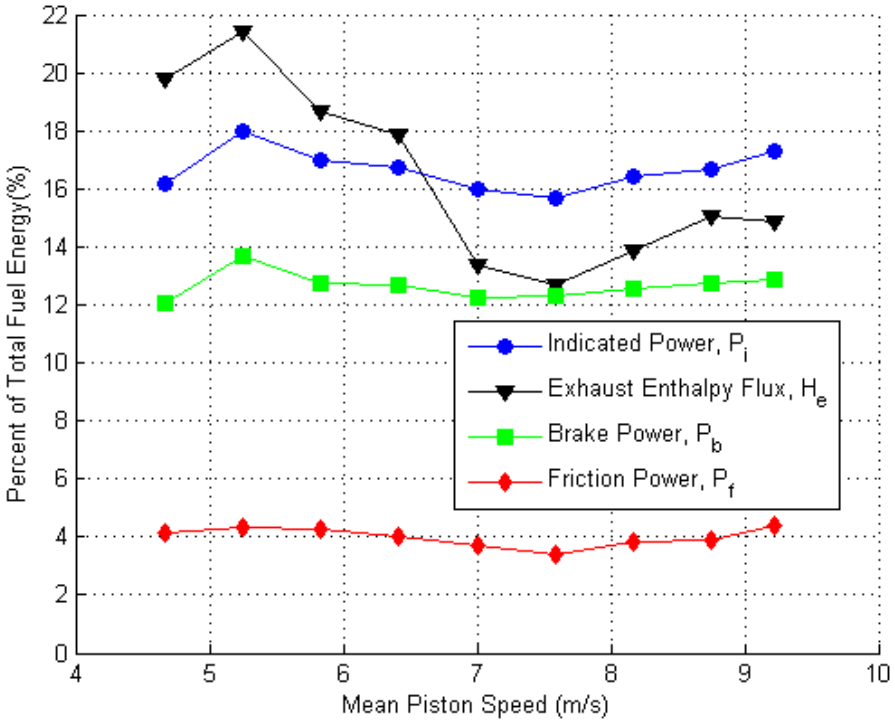

Figure 4.16: Power values as a percent of total fuel energy for Engine #3 at WOT

Values for short-circuiting and incomplete combustion were estimated from literature. Short circuiting was based on Heywood's mention of 20% of the fuel loss [6] and another author's range of 15-40% [14]. A linear model was used for the energy balance by combining these values with the knowledge that short-circuiting decreases with engine speed [7]. Short-circuiting loss was conservatively estimated at 25% at 4000 rpm with a linear decrease to 10% at 7900 rpm.

Incomplete combustion values were based on Figure 2.4 [6] and the measured equivalence ratios for Engine #3. At each data point, the measured equivalence ratio value was compared to Figure 2.4 to estimate an incomplete combustion loss. At WOT, the loss varied approximately linear from 5% loss at 4000 rpm up to 23% loss at 7900 rpm. At the

25% power setting the values ranged from 5% at 4000 rpm, peaking at 25% near 6000 rpm before falling to 11% at 7900 rpm.

A summation plot of the energy values in Equation 4.5 was then developed as shown in Figures 4.17 and 4.18. The energy values as a percent of total fuel energy are added to one another as in the equation. The gap between the top of the summed values and 100% of the fuel is the approximated heat rejection. At WOT, Figure 4.17 approximates heat rejection at 30-40%. At the 25% power setting, Figure 4.18 approximates heat rejection at 27-40%.

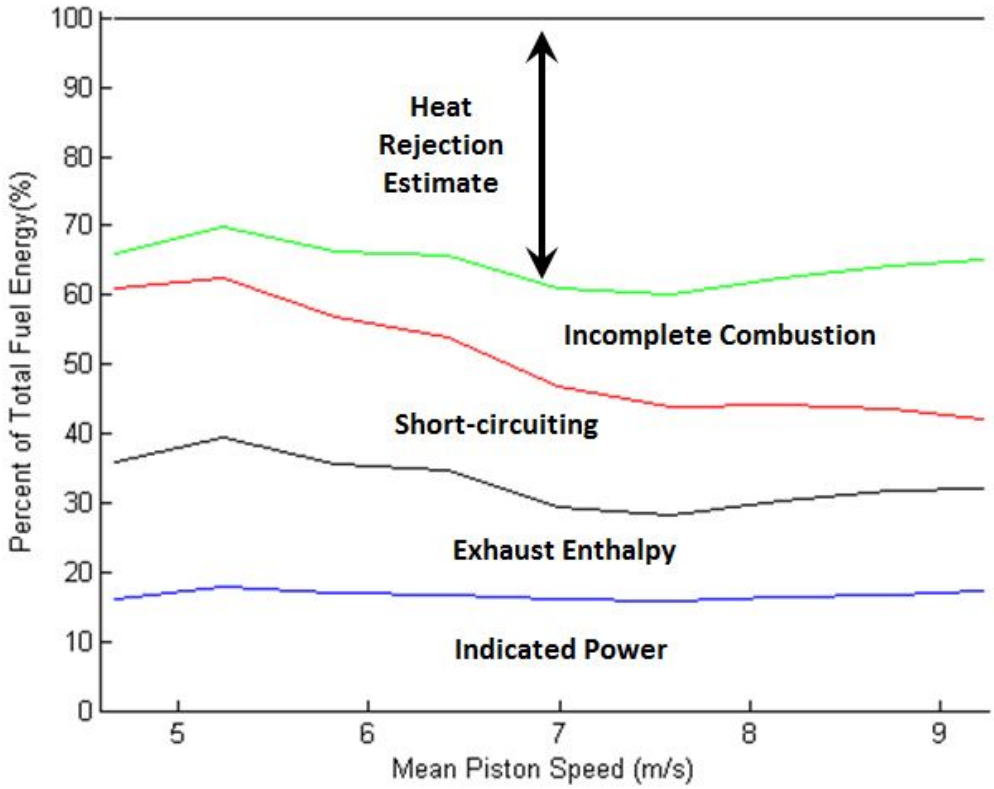

Figure 4.17: Sum of energy values leaving Engine #3 at WOT

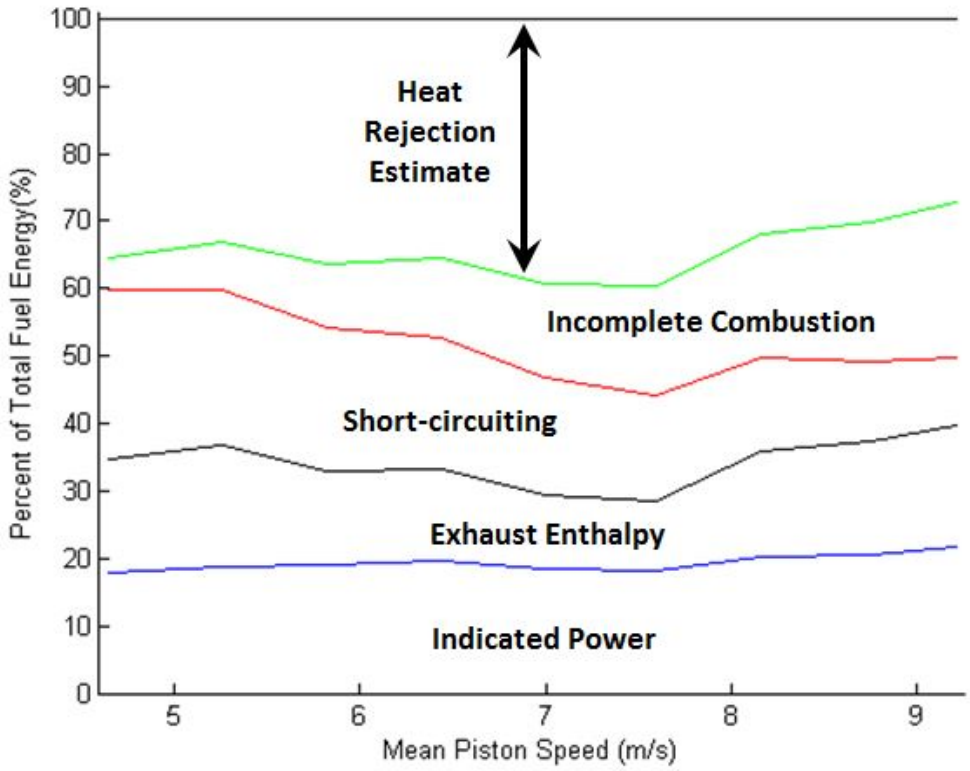

Figure 4.18: Sum of energy values leaving Engine #3 at 25% power

4.3 Monitoring Heat Loss to External Engine Flow Results

This section describes the data and analysis for measuring the enthalpy increase of the air blowing across the outside of the cylinder body. The setup for this method was completed prior to testing Engines #2 and #3. This allowed data for this method to be collected concurrently with the other test methods. The test matrix was concurrent with the energy balance method in that the engine was tested from 4000 rpm up to 7900 rpm (4.7-9.2 $\frac{\text{m}}{\text{s}}$ mean piston speed, $\bar{S}_p$). At each speed, measurements were taken at throttle settings that provided maximum brake power (100%), 75%, 50%, and 25% power.

Thermal losses were measured using the engine enclosure and controlled airflow as shown in Figures 3.9 & 3.11. Heat rejection measurements with and without the rigid

insulation is shown in Figure 4.19. Placement of the insulation was inside the enclosure as seen in Figure 3.12. The figure shows that there is no significant increase in heat rejection measurements with the added insulation. The insulation did however provide more control over engine temperature. The increased control was most likely the result of increased air flow directed at the engine by the addition of the insulation.

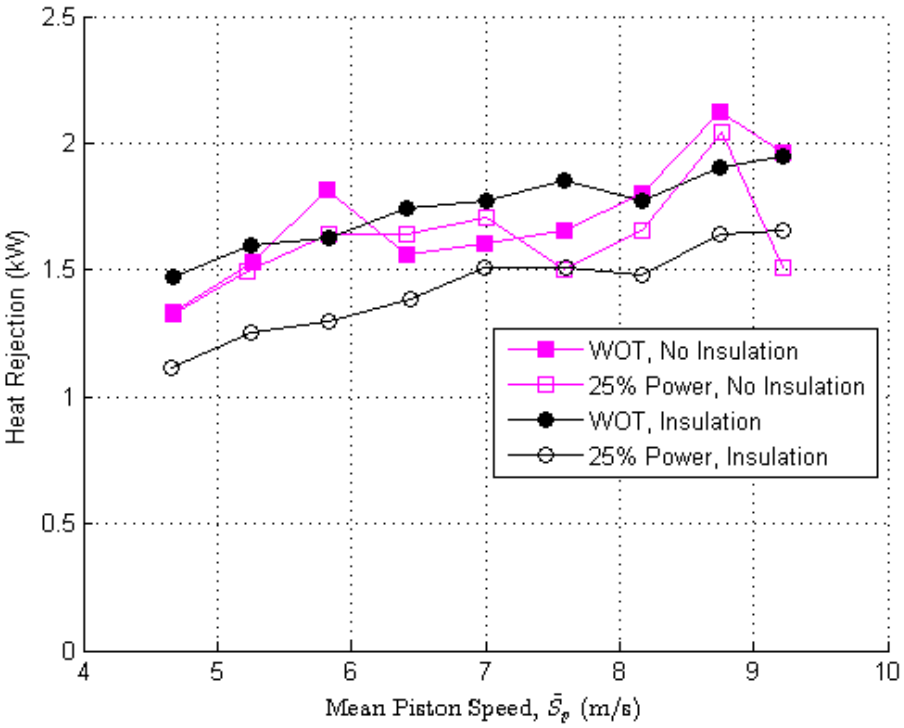

Figure 4.19: Heat rejection measurements of Engine #3 through enclosure at WOT and 25% power

Figure 4.20 shows the heat rejection values at the various power settings. There is a consistent increase in heat rejection of about 0.5 kW over the engine speed range. Maximum heat rejection of 1.9 kW is at WOT and 7900 rpm. Only slight differences

between the power settings exist with approximately 0.3 kW difference between WOT and the 25% power setting.

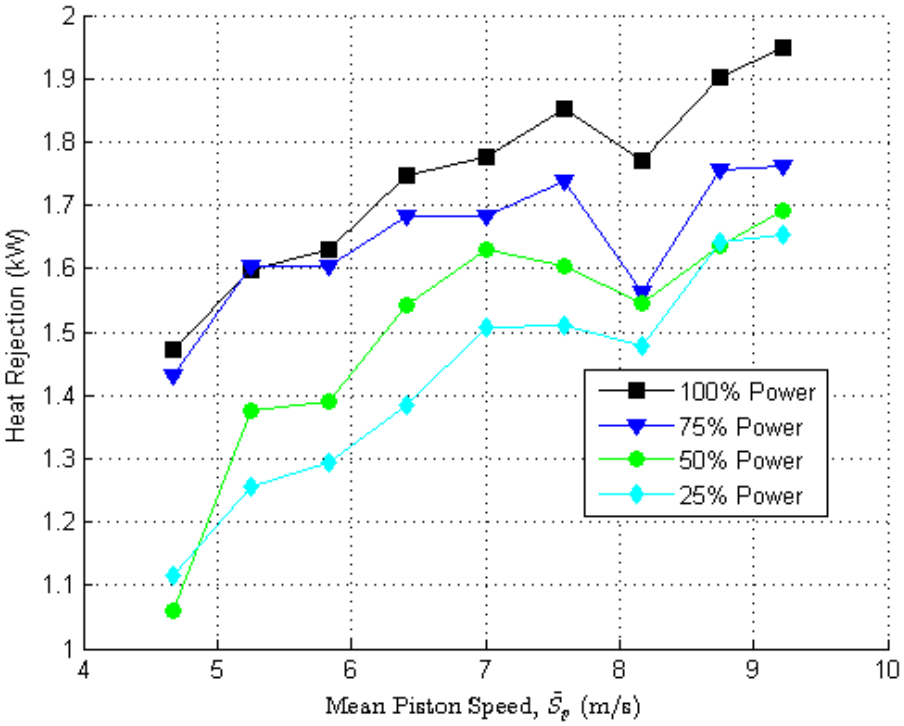

Figure 4.20: Heat rejection measurements for Engine #3

Figure 4.21 is an evaluation of these measurements as a percent of total fuel energy. The 25% power setting resulted in the largest heat rejection percentages at 20-26%. For the higher throttle settings the maximum heat rejection percentages occurred at the slowest engine speeds (4000-4500 rpm). At WOT, the heat rejection varied from 8-11% of the total fuel energy.

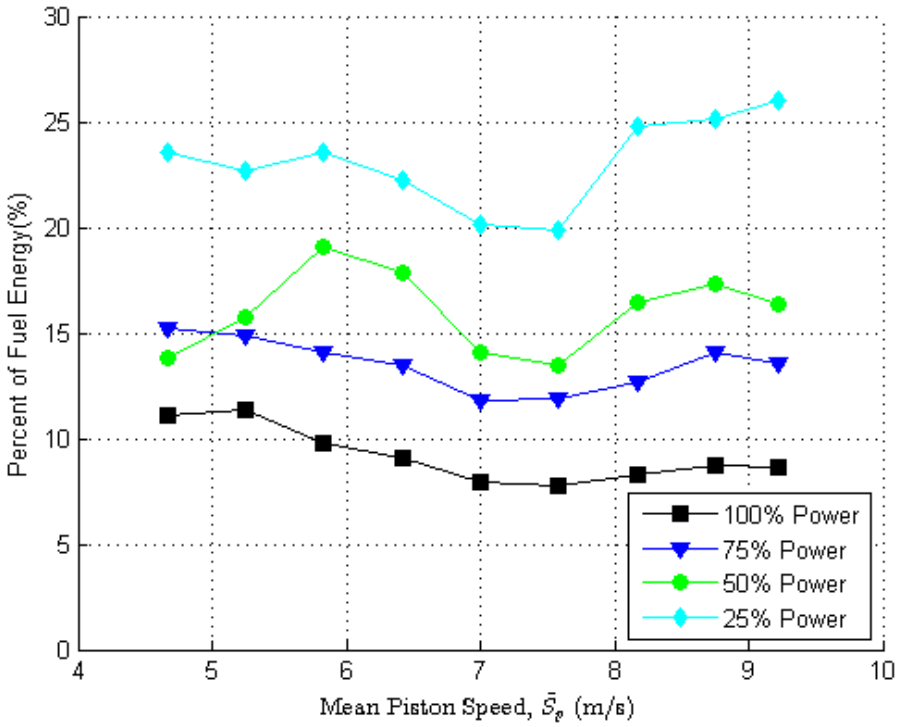

Figure 4.21: Heat rejection at partial loading as a percent of total fuel energy

The heat rejection measurements were further evaluated in comparison to the indicated power and exhaust enthalpy values. Figure 4.22 shows these values as a percent of the total fuel energy measured at each point.

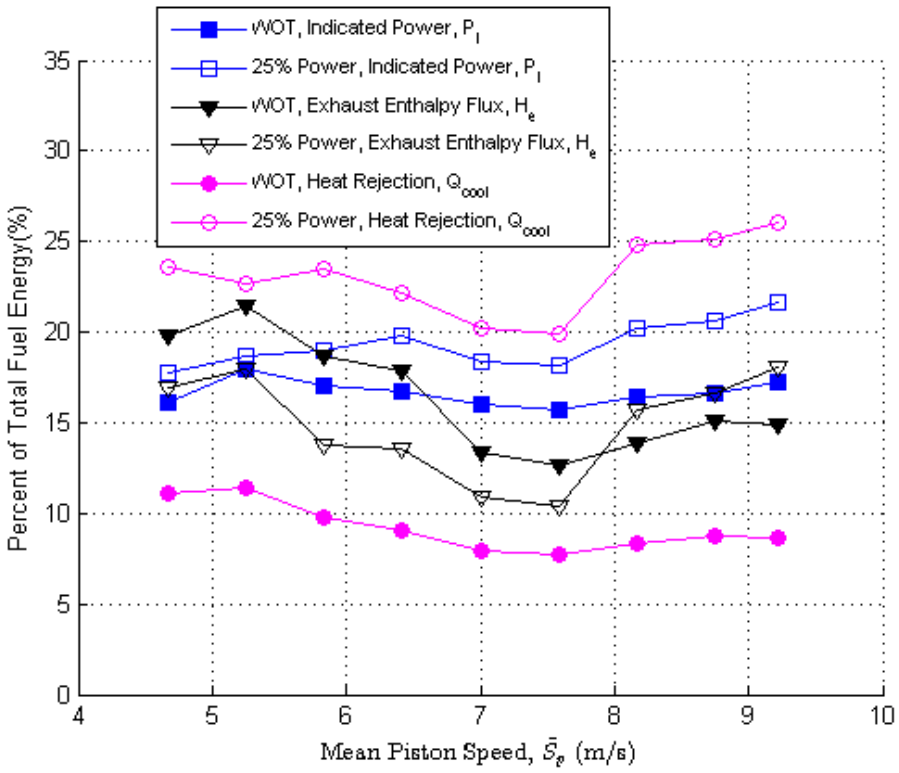

Figure 4.22: Indicated power, exhaust enthalpy, and heat rejection measurements for Engine #3

An additional test was performed with the blower and enclosure setup. The engine was held at a constant load condition of 6000 rpm and 50% power setting. The blower was brought to full speed while the thermocouple on the exhaust side of the engine was monitored. Data collection was done once the temperature settled. The blower setting was then reduced in 10% increments with data recorded at each step. The test ended when the exhaust side temperature would not hold a temperature of less than 150 °C. The results of this test are shown in Figure 4.23. As the blower power was increased there was a decrease in measured heat rejection of approximately 0.2 kW. At this operating condition this decrease equates to 2% of the total fuel energy. During this test there was no distinguishable change in brake power values.

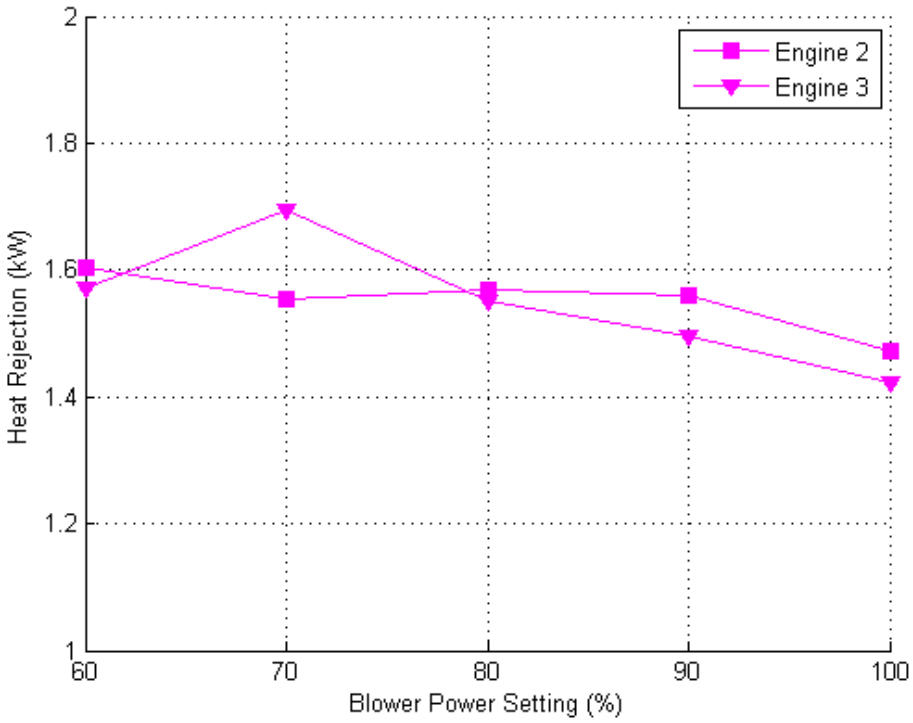

Figure 4.23: Heat rejection during 60-100% blower sweep at 6000 rpm, 50% power setting

4.4 Heat-Flux Gauge Measurement Results

The results and analysis in this section are related to measuring the heat flux on Engine #3. This engine was instrumented with thin-film heat flux gauges at three locations. The goal of this method was to collect direct measurements of heat flux ($\frac{kW}{m^2}$) and relate this to total thermal loss. This data was collected concurrently with the other two previous test methods at engine speeds from 4000 rpm up to 7900 rpm. At each speed, measurements were taken at throttle settings that provided maximum brake power (100%), 75%, 50%, and 25% power.

The heat flux gauge measurement method required repeated operational checks of the resistance. Operational resistance checks were performed by measuring the resistance of

each element at a known temperature. For this reason, a Type-E thermocouple was placed in close proximity to each of the heat flux gauges. With the engine at equilibrium with the ambient air temperature, both the resistances of the elements and the temperature of the corresponding thermocouples were recorded. These resistance and temperature values were used to find the R_0 values based on a linear resistance/temperature curve. Table 4.2 shows the amount of resistance change between test runs.

Table 4.2: Heat flux gauge operational checks

Gauge	Upstream	Upstream	Downstream	Downstream	Top	Top
Location	Upper	Lower	Upper	Lower	Upper	Lower
Coefficient, α_R ($\frac{1}{K}$)	0.001577275	0.001593	0.001645	0.001564	0.001550	0.001556
Pre-Run #1 (Ω), R_0	134.80	103.95	130.00	100.37	111.94	122.50
Post-Run #1 (Ω), R_0	134.49	103.83	129.71	100.21	112.24	122.05
ΔR_0 Run #1 (Ω), R_0	-0.31	-0.12	-0.29	-0.16	0.3	-0.45
Pre-Run #2 (Ω), R_0	134.69	103.93	130.04	100.30	112.04	122.03
Post-Run #2 (Ω), R_0	134.08	103.74	129.68	99.74	112.84	121.67
ΔR_0 Run #2 (Ω), R_0	-0.61	-0.19	-0.36	-0.56	0.80	-0.36
Pre-Run #3 (Ω), R_0	134.08	103.74	129.68	99.74	112.84	121.67
Post-Run #3 (Ω), R_0	134.46	103.68	129.79	99.63	113.08	121.31
ΔR_0 Run #3 (Ω), R_0	0.38	-0.06	0.11	-0.11	0.24	-0.36

During test runs, the gauge elements measured temperatures as low as 10 °C before start-up and as high as 200 °C during operation. This 190 °C temperature difference during a test run results in a gauge resistance change of approximately 40 Ω. The largest change in the R_0 resistance between pre and post test run checks was +0.8 Ω found in the gauge at the top of the cylinder during Run #2. A change in resistance of 0.8 Ω corresponds to a

temperature difference of 3.8 °C and a change in heat flux of 13.2 $\frac{\text{kW}}{\text{m}^2}$. The majority of the gauges however changed approximately 0.35 Ω or less resulting in a heat flux change of 5.8 $\frac{\text{kW}}{\text{m}^2}$.

The IR camera was used once again, this time to view the engine running with the heat flux gauges installed. Figure 4.24 is a top-down view of the engine. A standard image of this same view is provided in Figure 4.25 for comparison to the IR image. The temperature distribution is seen to be relatively uniform except for locations where wiring or bolts are added. The temperature difference at these locations is likely more pronounced due to different emissivities compared to that of the weathered aluminum cylinder body.

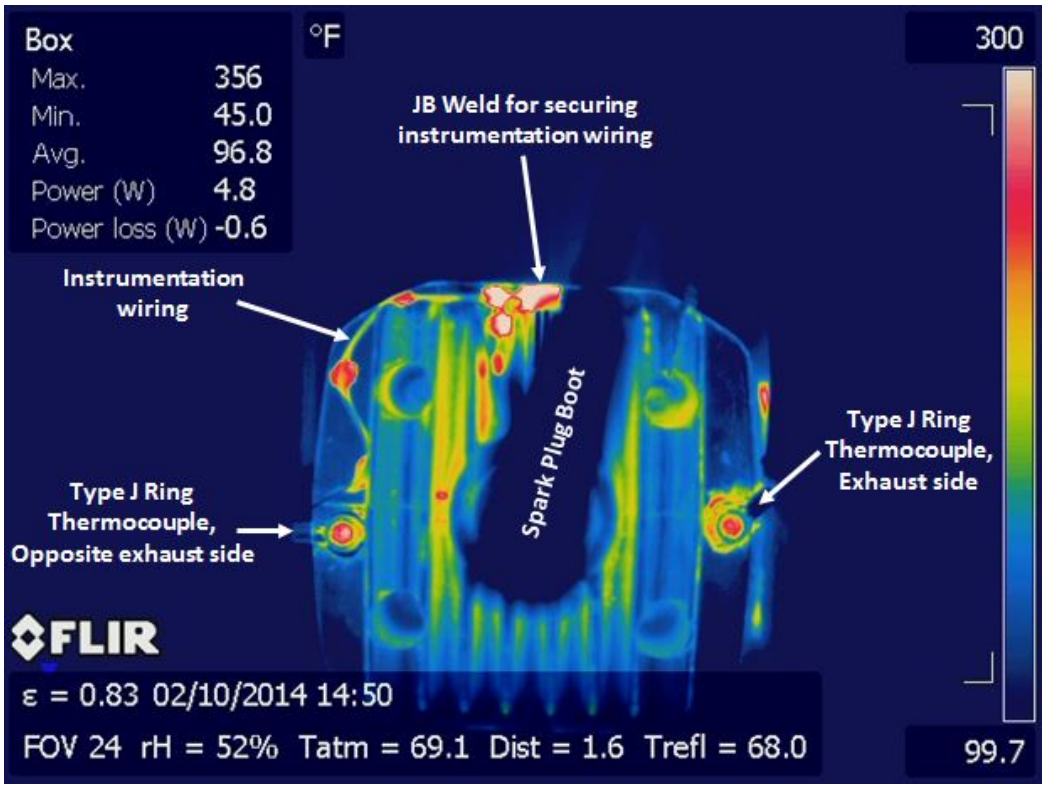

Figure 4.24: IR image of Engine #3 cylinder head with thin-film heat flux gauge installed.

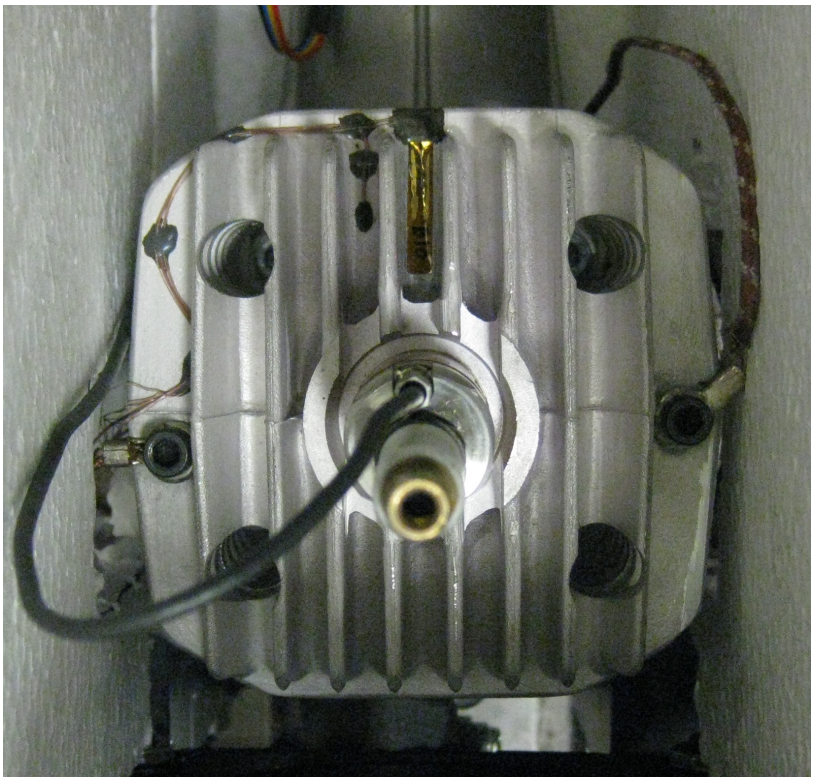

Figure 4.25: Image of Engine #3 cylinder head with thin-film heat flux gauge installed and spark plug boot removed

The temperatures measured from each element of the heat flux gauges are plotted in Figure 4.26 along with the corresponding thermocouple temperatures. The lower gauge element and thermocouple at the top of the cylinder head measured the highest temperatures with a maximum of 202 °C at 9.2 $\frac{m}{s}$. The upper gauge element was the element exposed to the air flow and consistently measured approximately 9 °C lower than the lower element and thermocouple. A similar temperature difference of 9 °C was observed between the downstream heat flux gauge elements. The thermocouple located near the downstream gauge however measured temperatures consistently higher than the lower gauge element. The higher reading is likely a result of thermocouple placement that is closer to the top of the cylinder head. The upstream heat flux gauge measured the lowest temperatures with a

maximum of only 136 °C at 9.2 $\frac{m}{s}$. There was almost no difference between the lower and upper gauge elements while the thermocouple measured temperatures approximately 15 °C higher.

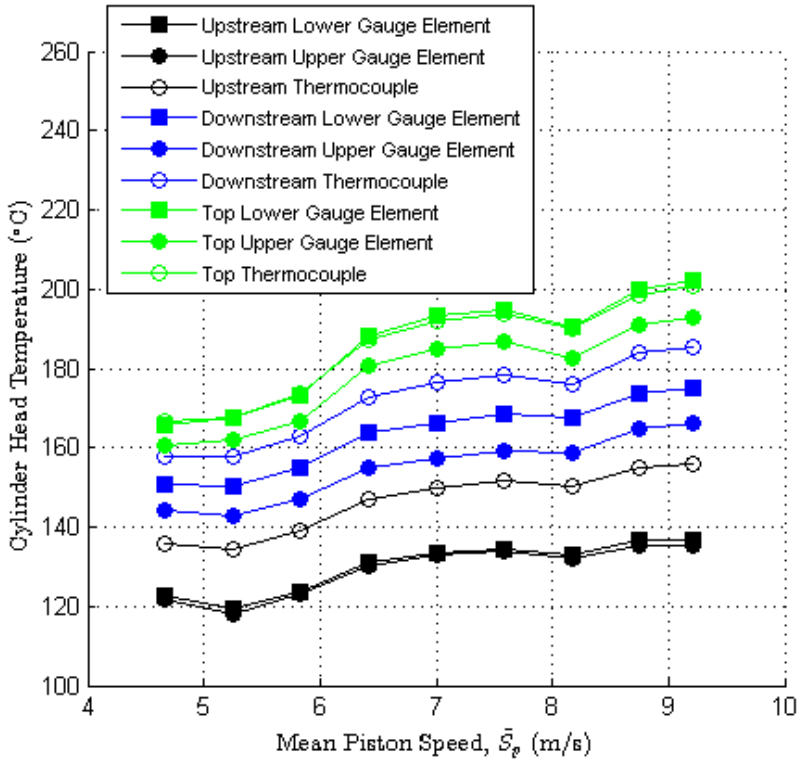

Figure 4.26: Heat flux gauge element and thermocouple temperatures of Engine #3 at WOT

The heat flux at the three locations was calculated using the measured temperature values of each gauge element and Equation 3.8. The measured heat flux values for each gauge and run of Engine #3 are shown in Figure 4.27. The heat flux gauges downstream of the airflow and at the top of the cylinder have the same trend at WOT, separated by approximately 5 $\frac{kW}{m^2}$ and then converging near the maximum engine speed. The heat flux measurements from the upstream gauge however are much lower with values ranging

from 2-5 $\frac{kW}{m^2}$. At the 25% power setting, the values from the downstream and top gauge overlap each other while the upstream gauge measures a negative value. Measurements from the upstream gauge are generally discarded moving forward because of the very low and negative measurements. From the downstream and top gauges, heat flux increases with engine speed. This increase with engine speed was also seen in the external airflow measurements.

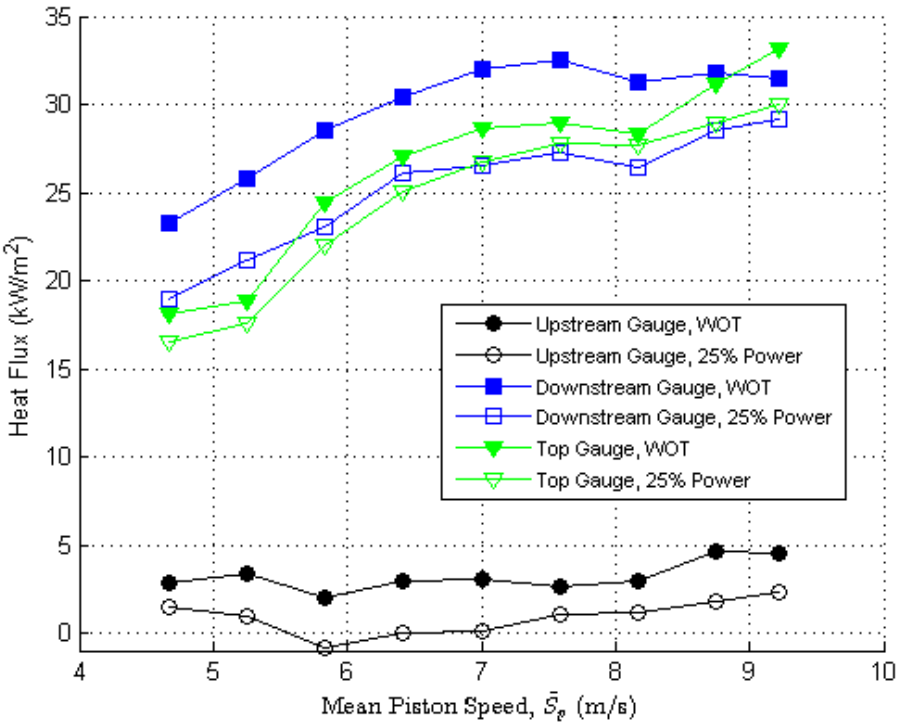

Figure 4.27: Measured heat flux values of Engine #3

Total heat rejection values are shown in Figure 4.28. These values use an exterior cylinder surface area of 640 cm^2 and assume a uniform heat flux distribution on the cylinder body. At WOT, the heat rejection ranges from 1.2 at 4000 rpm up to 2.1 at 7900 rpm.

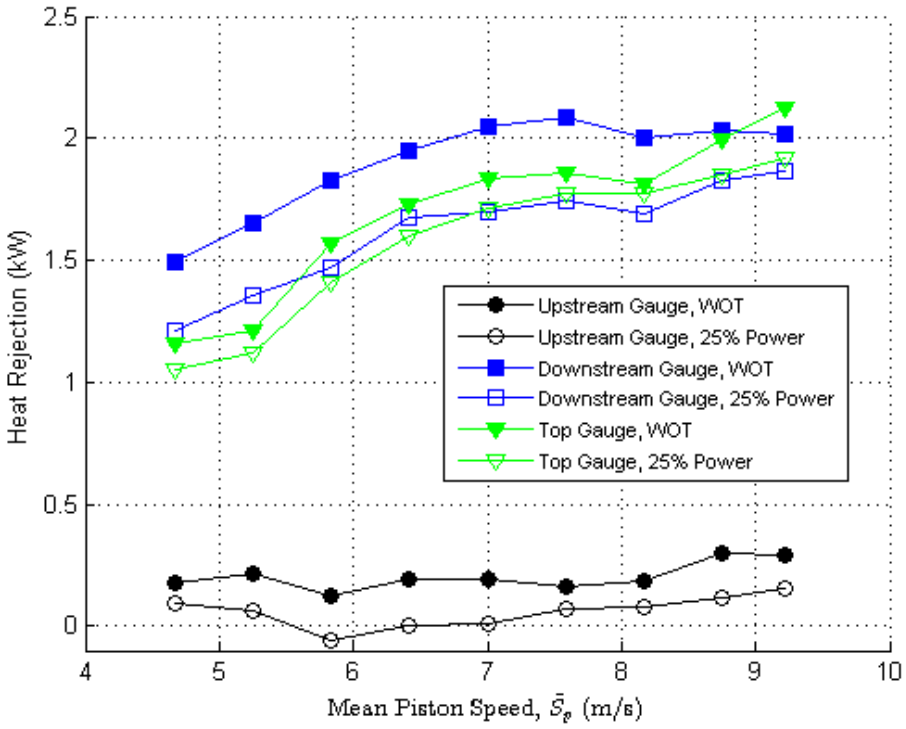

Figure 4.28: Heat rejection of Engine #3 assuming uniform heat flux

The heat rejection values were also evaluated as a fraction of the total fuel energy coming into the engine. These percentages shown in Figure 4.29 show fairly constant values over the speed range. The values for the downstream and top gauges at WOT range from 7-13 % of total fuel energy. This compares to 8-11 % as measured in the external flow method.

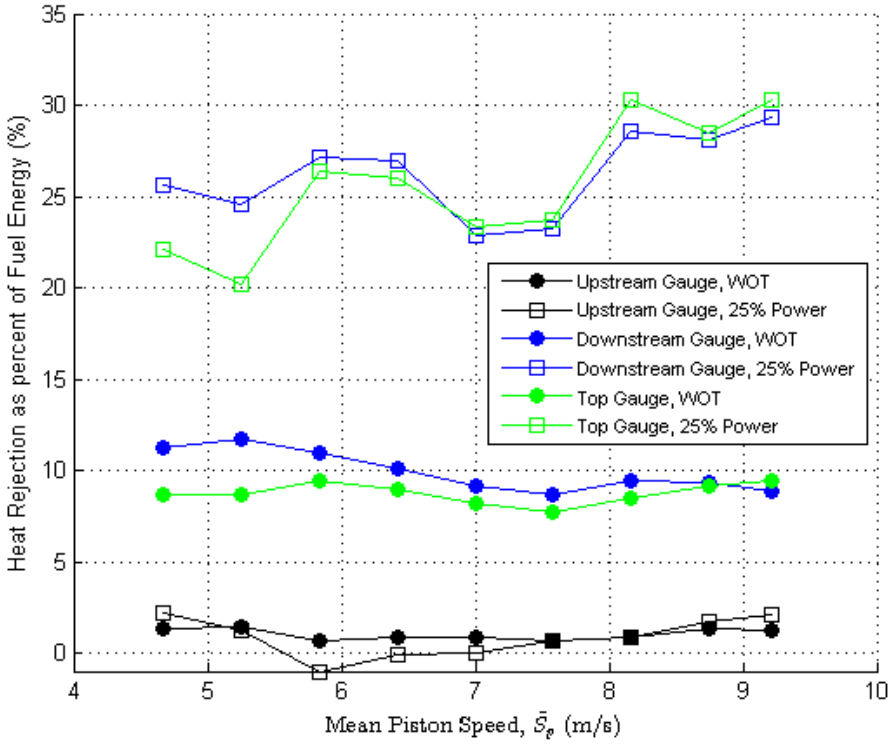

Figure 4.29: Heat rejection of Engine #3 as a fraction of total fuel energy and assuming uniform heat flux

An average between the downstream and top gauge was taken for each of the power settings. Figure 4.30 shows the heat rejection values from the average at 100%, 75%, 50%, and 25% power settings. Similar to the external flow measurements, heat rejection percentages increase as the power setting decreases. Heat rejection for the 25% power setting range from 22-30% of the total fuel energy compared to the 20-26% measured in the external flow method.

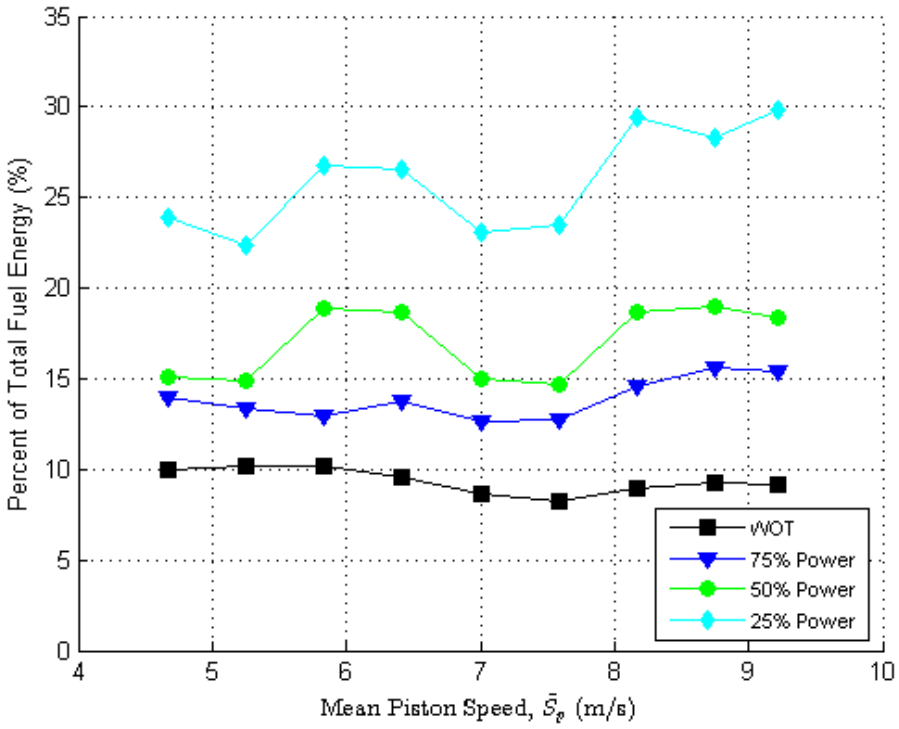

Figure 4.30: Heat rejection of Engine #3 at partial throttles as a fraction of total fuel energy and assuming uniform heat flux

The power values were again evaluated in comparison to the indicated power and exhaust enthalpy as was done with the external flow method. Figure 4.31 shows the resulting values using the averaged data from the downstream and top gauge. This is the same engine and test runs as the evaluation with the external flow in Figure 4.22.

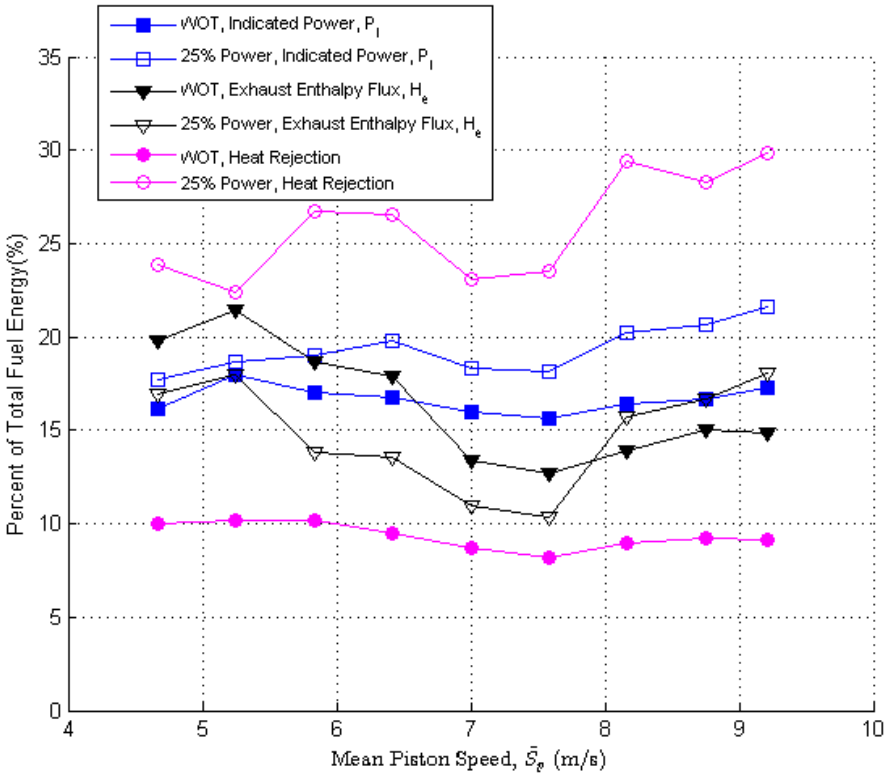

Figure 4.31: Heat rejection of Engine #3 assuming uniform heat flux

4.5 Comparison of Methods

The three measurement techniques varied in their results and level of difficulty. The objective of the energy balance method was to estimate heat rejection by accounting for all energy flow paths. The external flow method was conceptually simple yet required the construction of an engine enclosure. The heat flux gauge method was a very direct measurement but resulted in discrete values for heat flux.

The results of each method at full power are plotted in Figure 4.32. This comparison was based on measurements taken on Engine #3 since this is the only engine which utilized all three measurement techniques. The energy balance estimate (in black) ranges from 31-42% of the total fuel energy. The external flow and heat flux gauge measurements are

considerably lower than the energy balance estimates, but both overlap at 8-11% of the total fuel energy.

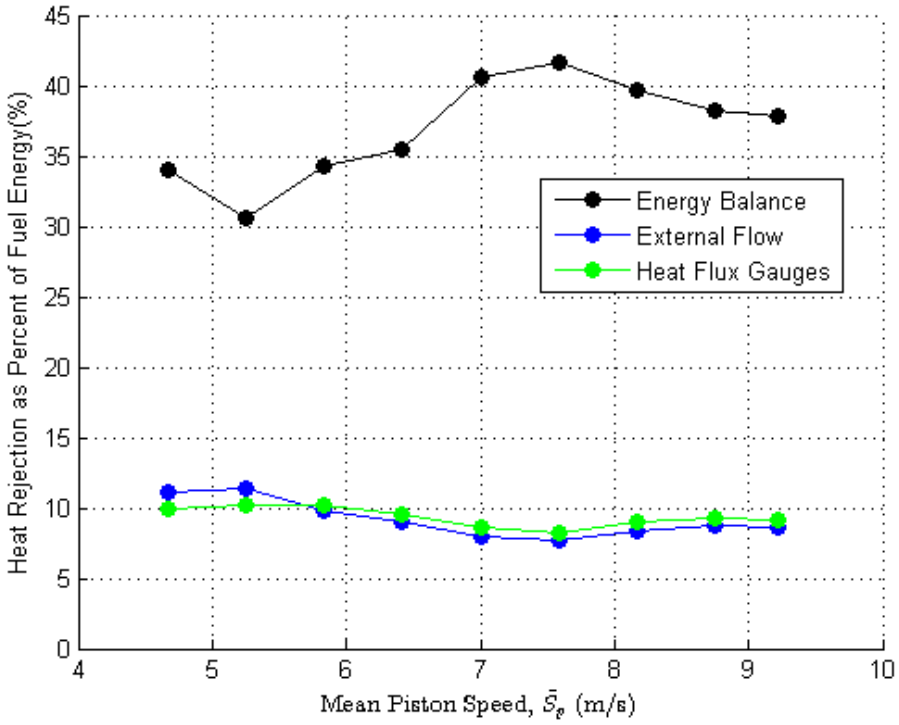

Figure 4.32: Comparison of heat rejection measurements for Engine #3 at WOT

A comparison at the 25% power setting is shown in Figure 4.33. The energy balance method estimate remains higher than the other methods at 27-40%, similar to the estimate at full power. The external flow method ranges from 20-26% of the total fuel energy. The heat flux gauge method starts out the same as the external flow method at lower engine speeds, then diverges by a few percent above. The heat flux gauge method resulted in a heat rejection of 22-30% of the total fuel energy. These readings show that a higher

percentage of the incoming energy goes to thermal loss for lower power settings compared to a full power setting.

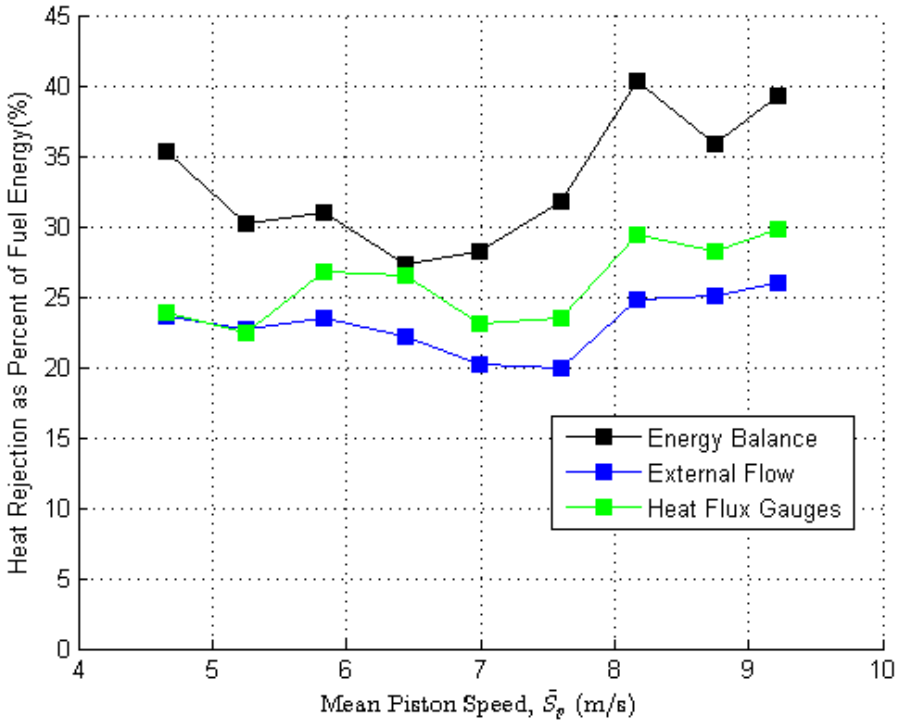

Figure 4.33: Comparison of heat rejection measurements for Engine #3 at the 25% power setting

A summation of the energy values leaving the engine is shown again but with the measured heat rejection values. Figure 4.34 shows the energy sum of Engine #3 at WOT. The heat rejection from the external flow method is shown in the magenta line and the cyan line shows the measurement from the heat flux gauge method. Unfortunately, the measurements only bring the sum to within 20-30% of having full accountability of the energy leaving the system.

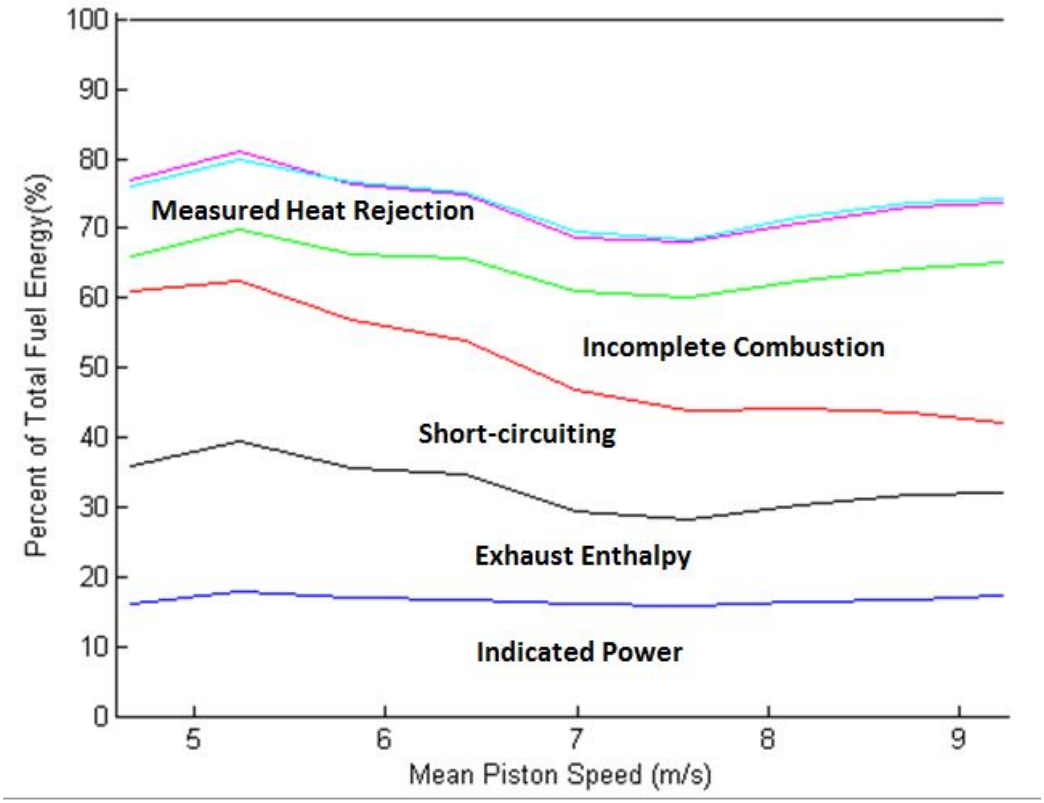

Figure 4.34: Sum of final energy values leaving Engine #3 at WOT

Figure 4.35 shows the energy sum of Engine #3 at the 25% power setting. The measurements from the external flow and heat flux gauge method bring the energy sum much closer to full accountability. The values used for short-circuiting and incomplete combustion are still estimates. These values could be improved with an emissions analysis that quantifies the amount of unburned hydrocarbons present in the exhaust.

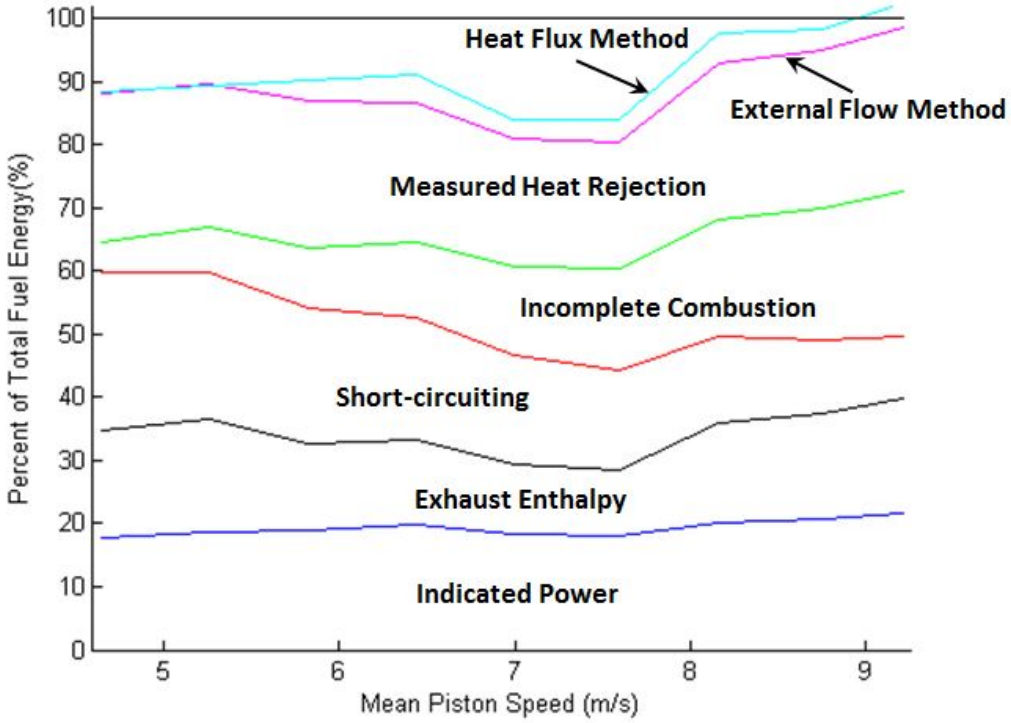

Figure 4.35: Sum of final energy values leaving Engine #3 at the 25% power setting

V. Conclusions and Recommendations

5.1 Research Conclusions

This effort focused on measuring thermal energy losses of a representative RPA engine using three measurement techniques. The engine chosen was the 3W-55i, a two-stroke spark-ignition engine with a surface area to displacement volume ratio of 1.48 $\frac{1}{\text{cm}}$. This surface area to displacement volume ratio is near the point where power output drops significantly as engine size is decreased. The first method performed an energy balance between the total fuel energy entering the engine and the various paths for energy to leave the engine. The second method measured the change in enthalpy as air was ducted through a box that enclosed the engine. The third method used thin-film heat flux gauges to measure the heat flux at three locations on the cylinder body. These measurements were combined with a qualitative analysis of IR images to calculate the total heat loss of the cylinder.

The three 55 cc engines tested were found to have an effective compression ratio of 7.4:1 resulting in an ideal fuel conversion efficiency of 50.4%. Actual maximum efficiency was found to be 13.7% at WOT and 4500 rpm for Engine #3. Maximum brake power was 2.9 kW at WOT and 6500 rpm, 0.9 kW less than the manufacturer rated power of 3.9 kW. Excluding drivetrain friction would reduce this difference. The total friction of the internal engine components and pumping losses combined with the drivetrain friction increased with engine speed and varied from 0.5-1.0 kW.

The energy balance method was based on measurements of fuel flow, indicated power, and exhaust enthalpy. The energy difference between the total fuel energy and the sum of the indicated power, exhaust enthalpy, short-circuiting, and incomplete combustion set the maximum value of energy that could be lost as heat rejection. These heat rejection values ranged from 30-40% of the total fuel energy while operating at WOT.

The external flow with engine enclosure method measured the flow rate and temperature difference of air flowing through a box that enclosed the engine. Heat rejection was measured to be approximately 1.9 kW while operating at WOT. This represented only 8-11% of the total fuel energy. When operated at 25% power settings, this method measured 20-26% of the total fuel energy.

The heat flux gauge method used three thin-film heat flux gauges to measure the heat flux on the cylinder body. The gauge facing the cooling air flow measured unreasonably low values around 0 $\frac{kW}{m^2}$. The other two gauges located at the backside of the engine and at the top of the engine measured values ranging from 18-33 $\frac{kW}{m^2}$. Using these values and the cylinder surface area, the resulting total heat rejection measured 1.2-2.1 kW. This amounts to 7-13% of the total fuel energy. At the 25% power setting, this method measured 22-30% of the total fuel energy.

The energy balance method was able to provide an approximate value for the thermal loss or heat rejection while the other two methods provided more direct measurements. The external flow method and heat flux gauge method results were similar to each other, but lower than the energy balance. The energy balance results could possibly be brought closer to the other methods with an emissions analysis of unburned fuel.

5.2 Recommended Future Research

Areas of improvement and additional research were identified during the execution of this testing effort. The small engine research effort will be continued by Alex Rowton and Joseph Ausserer. Their focus will shift from the 55 cc engine to the 28 cc and 85 cc 3W-Modelmotoren engines. On all of these engines, additional emissions instrumentation should be added to analyze and quantify the short-circuiting and incomplete combustion. This effort could be complemented with the addition of an exhaust system specifically tuned to reduce this short-circuiting losses. After initial baseline performance testing is performed, the spark timing could be optimized to achieve maximum performance and

efficiency. A port fuel-injection system could be added for increased control on the air/fuel mixture. Direct fuel-injection would be a step further in that short-circuiting effects could also be minimized. Once a fuel injection system and a custom ignition control module is implemented, a switch to a low AKI fuel would be less troublesome. The capstone of the 3W-Modelmotoren engine effort would then be the combined implementation of direct-fuel injection, custom ignition timing, and tuned exhaust while running on a low AKI fuel to show higher efficiencies and decreased BSFC.

Bibliography

[1] 3W-Modellmotoren. "Engine Manual 55i / 55i CS". URL http://www.3w-modellmotoren.com. Accessed: 2013-05-13.

[2] Ajav, E., B. Singh, and T. Bhattacharya. "Thermal Balance of a Single Cylinder Diesel Engine Operating on Alternative Fuels". *Energy Conversion and Management*, 41(14):1533–1541, 2000.

[3] Ausserer, Joseph, Paul Litke, Jon-Russell Groenewegen, Alex Rowton, and Keith Grinstead. "Development of Test Bench and Characterization of Performance in Small Internal Combustion Engines". *Submitted for Publication*, 2013.

[4] Epstein, A., G. Guenette, R. Norton, and C. Yuzhang. "High-frequency response heat-flux gauge". *Review of Scientific Instruments*, 57(4):639–649, 1986.

[5] Groenewegen, Jon-Russell. *The Performance and Emissions Characteristics of Heavy Fuels in a Small, Spark Ignition Engine*. Master's thesis, University of Dayton, 2011.

[6] Heywood, John. *Internal Combustion Engine Fundamentals*, volume 930. McGraw-Hill New York, 1988.

[7] Heywood, John and Eran Sher. *The Two-Stroke Cycle Engine: Its Development, Operation, and Design*. Taylor & Francis, 1999.

[8] Husaboe, Travis. *Effects of Temperature on the Performance of a Small Internal Combustion Engine at Altitude*. Master's thesis, Air Force Institute of Technology, 2012.

[9] Kumarappa, S. and G. Prabhukumar. "Improving the Performance of Two Stroke Spark Ignition Engine by Direct Electronic CNG Injection". *Jordan Journal of Mechanical and Industrial Engineering*, 2(4):169, 2008.

[10] Martinez-Frias, Joel, Salvador Aceves, Daniel Flowers, J. Smith, and Robert Dibble. "HCCI Engine Control by Thermal Management". *SAE Transactions*, 109(4):2646–2655, 2000.

[11] Mueller, Torsten, Helmut Hans, Winfried Krebs, Stuart Smith, and Achim Koenigstein. "Thermal Management on Small Gasoline Engines". *SAE technical paper*, 2011-01-0314, 2011.

[12] NASA, Glenn Research Center. "Ideal Otto Cycle p-V diagram", July 2008. URL http://www.grc.nasa.gov/www/k-12/airplane/otto.html. Accessed: 2013-09-25.

[13] Obert, Edward. *Internal Combustion Engines and Air Pollution*. Intext Educational Publishers, 1973.

[14] Raghavendra-Rao, D. and B. Samaga. "Some Studies on the Scavenging Process in a Two-Stroke S. I. Engine". *11th National Conference on IC Engines and Combustion*, 375–384, 1989.

[15] Taylor, Charles Fayette. *The Internal-Combustion Engine in Theory and Practice: Combustion, Fuels, Materials, Design*, volume 2. The MIT press, 1985.

[16] Taylor, Charles Fayette. *The Internal-Combustion Engine in Theory and Practice: Thermodynamics, Fluid Flow, Performance*, volume 1. The MIT press, 1985.

[17] Turns, Stephen. *An Introduction to Combustion*. McGraw-Hill New York, 2000.

[18] Wilson, Cary. *Performance of a Small Internal Combustion Engine Using N-Heptane and Iso-Octane*. Master's thesis, Air Force Institute of Technology, 2010.

REPORT DOCUMENTATION PAGE

Form Approved
OMB No. 0704–0188

The public reporting burden for this collection of information is estimated to average 1 hour per response, including the time for reviewing instructions, searching existing data sources, gathering and maintaining the data needed, and completing and reviewing the collection of information. Send comments regarding this burden estimate or any other aspect of this collection of information, including suggestions for reducing this burden to Department of Defense, Washington Headquarters Services, Directorate for Information Operations and Reports (0704–0188), 1215 Jefferson Davis Highway, Suite 1204, Arlington, VA 22202–4302. Respondents should be aware that notwithstanding any other provision of law, no person shall be subject to any penalty for failing to comply with a collection of information if it does not display a currently valid OMB control number. **PLEASE DO NOT RETURN YOUR FORM TO THE ABOVE ADDRESS.**

1. REPORT DATE *(DD–MM–YYYY)*	2. REPORT TYPE	3. DATES COVERED *(From — To)*
27–03–2014	Master's Thesis	Oct 2012–Mar 2014

4. TITLE AND SUBTITLE

Thermal Loss Determination for a
Small Internal Combustion Engine

5a. CONTRACT NUMBER

5b. GRANT NUMBER

5c. PROGRAM ELEMENT NUMBER

6. AUTHOR(S)

Rittenhouse, Joshua A., Captain, USAF

5d. PROJECT NUMBER

5e. TASK NUMBER

5f. WORK UNIT NUMBER

7. PERFORMING ORGANIZATION NAME(S) AND ADDRESS(ES)

Air Force Institute of Technology
Graduate School of Engineering and Management (AFIT/EN)
2950 Hobson Way
WPAFB, OH 45433-7765

8. PERFORMING ORGANIZATION REPORT NUMBER

AFIT-ENY-14-M-41

9. SPONSORING / MONITORING AGENCY NAME(S) AND ADDRESS(ES)

Air Force Research Laboratory, Aerospace Systems Directorate
Attn: Dr. Fred Schauer
2130 Eighth Street, Bldg 45, Rm 190
WPAFB OH 45433-7542
Comm: 937-255-6462 (DSN: 785-6462) frederick.schauer@us.af.mil

10. SPONSOR/MONITOR'S ACRONYM(S)

AFRL/RQTC

11. SPONSOR/MONITOR'S REPORT NUMBER(S)

12. DISTRIBUTION / AVAILABILITY STATEMENT

DISTRIBUTION STATEMENT A:
APPROVED FOR PUBLIC RELEASE; DISTRIBUTION UNLIMITED

13. SUPPLEMENTARY NOTES

This work is declared a work of the U.S. Government and is not subject to copyright protection in the United States.

14. ABSTRACT

Three analysis techniques were used to measure the heat rejection of a 55 cc air-cooled two-stroke engine. This study was performed as part of a larger effort aimed at extending range and endurance limitations of Group 1 & 2 Remotely Piloted Aircraft (RPA). The engine selected for the study was a 55 cc gasoline-fueled, carbureted, spark-ignition engine made by 3W-Modellmotoren and is representative of RPA engines in these groups. With a surface area to volume ratio of 1.48 $\frac{1}{\text{cm}}$, the engine is in a size region where thermal losses begin to dominate engine efficiency and thermal efficiencies of less than 20% are common. The first measurement method was an energy balance between the fuel energy entering the system and the various avenues for energy to leave the system. The second method used an enclosure around the engine and measured the enthalpy increase of the air flowing past the cooling fins. The third method used heat flux gauges placed on the cylinder head to measure the heat flux at those locations. The energy balance method estimated heat rejection at approximately 30-40% of the total fuel energy for full and partial power settings. As part of the energy balance method, the engines tested achieved a maximum thermal efficiency of 13.7% and a maximum brake power value of 2.9 kW. The engine enclosure method measured heat rejection values to be approximately 2 kW at full and partial power settings. This equates to 8-11% of the fuel energy at full power and 20-26% at a 25% power setting. The heat flux gauge method measured heat flux values of up to 33 $\frac{\text{kW}}{\text{m}^2}$. Applying the heat flux values over the surface area of the cylinder resulted in 1.2-2.1 kW of heat loss. As a percent of total fuel energy this represents 7-13% at full power and 22-30% at a 25% power setting.

15. SUBJECT TERMS

Reciprocating two-stroke engine thermal loss

16. SECURITY CLASSIFICATION OF:			17. LIMITATION OF ABSTRACT	18. NUMBER OF PAGES	19a. NAME OF RESPONSIBLE PERSON
a. REPORT	b. ABSTRACT	c. THIS PAGE			Dr. Marc Polanka, AFIT/ENY
U	U	U	UU	102	19b. TELEPHONE NUMBER *(include area code)* (937) 255-3636 x4714 marc.polanka@afit.edu